Probabilistic retrieval of volcanic SO_2 layer height and cumulative mass loading using the Cross-track Infrared Sounder (CrIS)

David M. Hyman[1] and Michael J. Pavolonis[1,2]

[1]Cooperative Institute for Meteorological Satellite Studies (CIMSS), University of Wisconsin - Madison, WI
[2]National Oceanic and Atmospheric Administration (NOAA) Center for Satellite Applications and Research (STAR), Madison, WI

Correspondence: David M. Hyman (dave.hyman@ssec.wisc.edu)

Abstract. During most volcanic eruptions and many periods of volcanic unrest, detectable quantities of sulfur dioxide (SO_2) are injected into the atmosphere at a wide range of altitudes, from ground level to the lower stratosphere. Because the fine ash fraction of a volcanic plume is, at times, collocated with SO_2 emissions, global tracking of volcanic SO_2 is useful in tracking the hazard long after ash detection becomes dominated by noise. Typically, retrievals of SO_2 loading have relied heavily
5 on hyperspectral ultraviolet measurements. More recently, infrared sounders have provided additional loading measurements and estimates of the SO_2 layer altitude, adding significant value to real-time monitoring of volcanic emissions as well as climatological analyses. These methods leverage the relative simplicity of infrared radiative transfer calculations, providing fast and accurate physics-based retrievals of loading and altitude.

In this study, we detail a probabilistic enhancement of an infrared SO_2 retrieval method, based on a modified trace-gas
10 retrieval, to estimate SO_2 loading and altitude probabilistically using the Cross-track Infrared Sounder (CrIS) on the Joint Polar Satellite System (JPSS) series of satellites. The methodology requires the characterization of real SO_2-free spectra aggregated seasonally and spatially. The probabilistic approach replaces loading and altitude estimates with non-parametric probability density functions, fully quantifying the retrieval uncertainty. This framework adds significant value over basic loading and altitude retrieval because it can be readily incorporated into Monte Carlo forecasting of volcanic emission transport.

15 We highlight results including successes and challenges from analysis of several recent significant eruptions including the 22 June, 2019 eruption of Raikoke volcano, Kuril Islands; the mid-December, 2016 eruption of Bogoslof volcano; and the 26 June, 2018 eruption of Sierra Negra volcano, Galapagos Islands. This retrieval method is currently being implemented in the VOLcanic Cloud Analysis Toolkit (VOLCAT), where it will be used to generate additional cloud object properties for real-time detection, characterization, and tracking of volcanic clouds in support of aviation safety.

20 ## 1 Introduction

During most volcanic eruptions and many periods of volcanic unrest, detectable quantities of sulfur dioxide (SO_2) are injected into the atmosphere at a wide range of altitudes, from ground level to the lower stratosphere. Often early in eruptions the fine ash fraction of a volcanic plume is collocated with SO_2 emissions and so ash tracking can be performed by proxy; however, later ash and SO_2 tend to evolve along different trajectories due to subtly differences in altitude and removal processes (Karagulian et al.,

25 2010; Corradini et al., 2010; Sears et al., 2013; Moxnes et al., 2014). Early collocation of SO_2 and ash is highly significant for informing forward trajectory models (e.g., HYSPLIT) of volcanic clouds as is performed in response to Volcanic Ash Advisories (VAAs) reported by the global network of Volcanic Ash Advisory Centers (VAACs). Becasue fine ash and SO_2 eventually diverge along different trajectories, due in large part to altitude differences, layer height estimates are critical for ash and SO_2 cloud estimates. Although volcanic ash presents a demonstrated threat to aviation (e.g., ICAO, 2012; Casadevall,

30 1994; Prata and Rose, 2015; Guffanti et al., 2010), SO_2 also presents an aviation safety concern, mainly as a human health hazard and damage by sulfuric acid, as well as impacts on global climate and air quality (Chin and Jacob, 1996; Prata, 2009; Carn et al., 2009; Robock, 2000).

Globally, measurements of SO_2 loading have previously relied heavily on low-earth orbiting hyperspectral ultraviolet (UV) instruments including the Ozone Monitoring Instrument (OMI), Ozone Mapping and Profiler Suite (OMPS), and Global Ozone

35 Monitoring Experiment–2 (GOME-2) (e.g. Krotkov et al., 2010; Carn et al., 2017; Li et al., 2017; Theys et al., 2013). More recently, efforts to improve UV methods have focused on high-cadence UV measurements made from the Deep Space Climate Observatory - Earth Polychromatic Imaging Camera (DSCOVR-EPIC) at the Earth-Sun (L1) Lagrange point (Carn et al., 2018) as well as high spatial resolution SO_2 loading and limited layer height measurements from the Tropospheric Monitoring Instrument (TROPOMI) (Theys et al., 2019; Hedelt et al., 2019). In the last decade, infrared sounders such as the Infrared

40 Atmospheric Sounding Interferometer (IASI) have provided additional SO_2 loading measurements and estimates of the layer altitude, providing significant added value to real-time monitoring of volcanic emissions as well as climatological analyses (Walker et al., 2011, 2012; Carboni et al., 2012, 2016; Clarisse et al., 2014; Bauduin et al., 2016). These methods leverage the relative simplicity of infrared radiative transfer calculations, providing fast and accurate physics-based retrievals of loading and altitude. Furthermore, infrared methods enable global coverage throughout the year as opposed to UV-based methods which

45 require incident sunlight, limiting effectiveness at high latitudes during the polar night.

In this study, we detail a probabilistic enhancement of the infrared SO_2 retrieval method of Clarisse et al. (2014), based on a modified trace-gas retrieval (Walker et al., 2011) to estimate SO_2 loading and altitude probabilistically utilizing the Cross-track Infrared Sounder (CrIS) currently aboard the Suomi-NPP (SNPP) and NOAA-20 satellites as part of the Joint Polar Satellite System (JPSS). The NOAA Unique CrIS/ATMS Processing System (NUCAPS) already includes a retrieval of SO_2 from CrIS

50 data (Gambacorta, 2013); however, it is based on a heritage algorithm designed to estimate many trace gases from cloud cleared radiances in one retrieval whereas we focus more specifically on the problem of retrieving SO_2 in any background atmosphere from all available CrIS measurements. The methodology requires the characterization of the background mid-wave infrared spectrum of the SO_2-free atmosphere, which is done by collecting the statistics of more than 360 million SO_2-free CrIS spectra aggregated seasonally and spatially. The probabilistic approach replaces loading and altitude estimates with non-parametric

55 probability density functions, fully quantifying the retrieval uncertainty. This framework adds significant value because it can be readily incorporated into Monte Carlo forecasting of volcanic emission transport.

In this study we highlight results including successes and challenges from analysis of several recent significant eruptions including the 22 June, 2019 eruption of Raikoke volcano, Kuril Islands; the mid-December, 2016 eruption of Bogoslof volcano; and the 26 June, 2018 eruption of Sierra Negra volcano, Galapagos Islands. This retrieval method is currently being imple-

60   mented in the VOLcanic Cloud Analysis Toolkit (VOLCAT, https://volcano.ssec.wisc.edu/ ; Pavolonis et al., 2013, 2015a, b,
      2018), where it will be used to generate additional cloud object properties for real-time detection, characterization, and tracking
      of volcanic clouds in support of aviation safety.

2   Probabilistic SO$_2$ layer retrieval theory

2.1   Classical methods for height retrieval

65   As a preliminary we discuss several methods which we describe here as "classical". In fact these methods are relatively recent;
      however, they do not make full use of the probability spaces which we will exploit here. Previous analyses of the height
      and distribution of volanic SO$_2$ plumes using data from the Infrared Atmospheric Sounding Interferometer (IASI) instrument
      by Carboni et al. (2012), Clarisse et al. (2014), and Carboni et al. (2016) utilized the ability to linearize a forward radiative
      transfer model around a climatological mean state for the concentration of trace SO$_2$, a method originally outlined by Walker
70   et al. (2011). Employing the notation of Rodgers (2000), the theory of this retrieval relates a set of parameters governing the
      concentration of a trace gas (SO$_2$ in this case) comprising the true state ($\mathbf{x}$) to a set of measurements $\mathbf{y}$, typically brightness
      temperature spectra by a forward radiative transfer model $\mathbf{F}$. As in Pavolonis (2010), all radiative transfer model simulations
      used in this study were performed using the LBLDIS tool (Turner, 2005), which utilizes the Line-by-Line Radiative Transfer
      Model (LBLRTM; Clough and Iacono, 1995) to compute gaseous absorption and the Discrete Ordinate Radiative Transfer
75   (DISORT) model to complete the radiative transfer calculation (including multiple scattering).

      The above trace gas methods for infrared sensors rely on the ability to write the data and true state each as a sum of
      the climatological average $(\overline{\mathbf{y}}, \overline{\mathbf{x}})$ and an anomaly $(\widetilde{\mathbf{y}}, \widetilde{\mathbf{x}})$ as $\mathbf{y} = \overline{\mathbf{y}} + \widetilde{\mathbf{y}}$ and $\mathbf{x} = \overline{\mathbf{x}} + \widetilde{\mathbf{x}}$ respectively. Linearizing around the
      climatological average gives:

$$\overline{\mathbf{y}} + \widetilde{\mathbf{y}} = \mathbf{F}(\overline{\mathbf{x}}; \mathbf{u}) + \mathbf{K}\widetilde{\mathbf{x}} + \varepsilon_{tot} \qquad (1)$$

80   where $\mathbf{u}$ is a collection of best estimates of all auxiliary parameters necessary to the forward model including the state of
      the atmosphere, surface and the instrument. $\mathbf{K}$ is the Jacobian matrix of $\mathbf{F}$ linearized about $\overline{\mathbf{x}}$ and ε_{tot} is the total error
      associated with the measurement, linearization, and other surface and atmospheric properties (including clouds) that influence
      the measured radiances. Because it is inferred that $\overline{\mathbf{y}} = \mathbf{F}(\overline{\mathbf{x}}; \mathbf{u})$, the equation for the error can be written simply as

$$\varepsilon_{tot} = \widetilde{\mathbf{y}} - \mathbf{K}\widetilde{\mathbf{x}}. \qquad (2)$$

85   From this formula, the retrieval of $\widetilde{\mathbf{x}}$ can proceed either by maximum likelihood estimation, iterative methods such as Levenberg-
      Marquard and gradient descent algorithms, or other methods.

      The analysis of Carboni et al. (2012) imposed an *a priori* Gaussian vertical distribution over pressure coordinates for the
      SO$_2$ concentration, retrieving only the total column SO$_2$, the mean pressure and the standard deviation (spread). By contrast,
      Clarisse et al. (2014) developed a system in which the SO$_2$ is assumed to exist in a narrow layer and an iterative retrieval is

performed for the total column concentration. For a very narrow layer, the concentration profile of anomalous SO_2 (the true
state) can be represented with the Dirac delta function of height:

$$\widetilde{\mathbf{x}} = x\delta(h - h_0) \tag{3}$$

where the gas of mass loading x is concentrated at the altitude h_0. In reality, the layer has some thickness and the concentration
is non-uniform. However, this abstraction is made for the benefit of complex probability calculations to follow. Using this form
of the concentration profile, the model spectrum is then a function of the mass loading and the layer height. Because the model
Jacobian for the trace gas retrieval is calculated at the background state, the Jacobian is the limit

$$\mathbf{K} = \mathbf{K}(\bar{x}, h_0) := \lim_{\epsilon \to 0} \frac{\mathbf{F}\big[(\bar{x}+\epsilon)\delta(h-h_0); \mathbf{u}\big] - \mathbf{F}\big[\bar{x}\delta(h-h_0); \mathbf{u}\big]}{\epsilon}. \tag{4}$$

For SO_2, the climatological background state ($\bar{x}$) is taken to be zero. In practice, calculating the limit is computationally
prohibitive so the limit is dropped and the perturbation (ϵ) is taken as 5 DU. Below we refer to the height-dependent Jacobian
calculated at the zero-background simply as $\mathbf{K}(h)$. Additionally, radiative transfer models do not have an implementation of
the Dirac delta, and consequently, a layer of finite thickness (1 km) is used which is an approximation to the Dirac delta.

Following Clarisse et al. (2014), this Jacobian can be used to calculate a height-dependent statistical z-score, measuring the
relative confidence in the state estimate:

$$z(h; \mathbf{y}, \overline{\mathbf{y}}) = [\mathbf{K}^{\mathsf{T}}(h)\mathbf{S}^{-1}\mathbf{K}(h)]^{-\frac{1}{2}}\mathbf{K}^{\mathsf{T}}(h)\mathbf{S}^{-1}(\mathbf{y} - \overline{\mathbf{y}}) \tag{5}$$

where the error covariance matrix $\mathbf{S}$ is built up from spectral residuals ($\mathbf{y} - \overline{\mathbf{y}}$) on measurements with low or no detectable
SO_2 present. The criteria for this discrimination are detailed in a later section. Note that the factor $\mathbf{K}^{\mathsf{T}}(h)\mathbf{S}^{-1}\mathbf{K}(h)$ is a scalar
at each height h. Here, $z(h; \mathbf{y}, \overline{\mathbf{y}})$ is the statistical z-score (number of standard deviations from the mean) of finding the SO_2
anomaly at elevation h given the data $\mathbf{y}$ and linearization about the mean spectrum $\overline{\mathbf{y}}$. Using this z-score function of height,
Clarisse et al. (2014) estimated the layer height (which we refer to as h_C) as that which maximizes the z-score function:

$$h_C := \arg\max_h z(h; \mathbf{y}, \overline{\mathbf{y}}). \tag{6}$$

Throughout the remainder of this work we use a functional notation to describe this height retrieval:

$$h_C = g(\mathbf{y}, \overline{\mathbf{y}}) = \arg\max_h z(h; \mathbf{y}, \overline{\mathbf{y}}). \tag{7}$$

2.2 Probabilistic enhancement

Although the classical methods make use of maximum likelihood estimation and are therefore probabilistic in the sense that
they retrieve the maximum likelihood estimate and the retrieval uncertainty estimate, they make an assumption of normality
about the input and output variables. Although this is workable for many types of retrieval, it is unsuitable for the height
retrieval in particular as follows. Instead of calculating the mean and covariance of the climatological background, we treat the
background spectrum as a random vector $\mathbf{Y}$, where the channels (each of the sampled wavenumbers) are correlated random

variables, each characterized by its own marginal probability distribution. In reality, these distributions may belong to a family of parameterized distributions; however, in this study they are non-parametric, only characterized by a histogram on each channel and a covariance structure:

$$\mathbf{S} = \mathbb{E}\Big[(\mathbf{Y} - \mathbb{E}[\mathbf{Y}])(\mathbf{Y} - \mathbb{E}[\mathbf{Y}])^{\mathsf{T}}\Big] \tag{8}$$

where the expectation operator is approximated by averaging over all samples. In this framework, the z-score function is a conditional random variable given the layer height h:

$$Z(h; \mathbf{y}, \mathbf{Y}) = Z | H{=}h \; = \; [\mathbf{K}^{\mathsf{T}}(h)\mathbf{S}^{-1}\mathbf{K}(h)]^{-\frac{1}{2}} \mathbf{K}^{\mathsf{T}}(h)\mathbf{S}^{-1}(\mathbf{y} - \mathbf{Y}) \tag{9}$$

and the height is a random variable:

$$H := g(\mathbf{y}, \mathbf{Y}). \tag{10}$$

The underlying assumption made by the classical method of Clarisse et al. (2014) is that $\mathbf{Y}$ is a multivariate normal random vector with mean $\overline{\mathbf{y}} = \mathbb{E}[\mathbf{Y}]$ and covariance $\mathbf{S}$, meaning that Z is a standard normal random variable ($Z \sim \mathcal{N}(0,1)$). This fact about the z-score is expected to hold in the present case with the full probabilistic characterization of $\mathbf{Y}$ which may not be Gaussian because the z-score is the sum over all of the channels in $bvecY$. The principal enhancement over the classical method comes from the height retrieval. Because the function g is highly nonlinear, due to the $\arg\max$ function, in general the mean height is not equal to the height calculated by Clarisse et al. (2014), that is

$$\mathbb{E}[H] = \mathbb{E}[g(\mathbf{y}, \mathbf{Y})] \neq g(\mathbf{y}, \mathbb{E}[\mathbf{Y}]) = h_C. \tag{11}$$

Furthermore, h_C is not generally the maximum likelihood height either ($h_C \neq \mathrm{mode}[H]$). Consequently, without a clear understanding of what h_C is measuring in terms of statistics, its probability distribution is unknown.

This study aims to estimate the probability distribution of H and show the importance of its probability density function (PDF) in making predictions about the cloud. We enhance the method of Clarisse et al. (2014), by retrieving a probabilistic SO_2 layer, that is, we retrieve the SO_2 layer height as a random variable H (Fig. 1).

In practice, we retrieve this PDF in a Bayesian framework. In this framework, we represent the height PDF as the posterior distribution due to a prior estimate $f_H^{prior}(h)$ of the distribution and a likelihood function $\mathcal{L}(h; \mathbf{y})$ based on the data (evidence). The likelihood function is constructed by Monte-Carlo (MC) sampling of $\mathbf{Y}$ and retrieving the height due to a background spectrum given by MC random sampling according to the marginal PDFs of $\mathbf{Y}$ and its covariance $\mathbf{S}$ (Fig. 1). The process for sampling this non-Gaussian correlated random vector is detailed in Appendix A. In this study we generate 10,000 samples of $\mathbf{Y}$ each denoted $\mathbf{y}^s \in \Omega_{\mathbf{Y}}$ where $\Omega_{\mathbf{Y}}$ is the sample space of $\mathbf{Y}$. Each height sample is generated as:

$$h^s = g(\mathbf{y}, \mathbf{y}^s), \tag{12}$$

that is we construct the random variable from elements of the sample space $h^s \in \Omega_H$. The likelihood function is then reconstructed by kernel density estimation (KDE) of these height samples, that is

$$\mathcal{L}(h; \mathbf{y}) = \mathrm{KDE}(\{h^s\}). \tag{13}$$
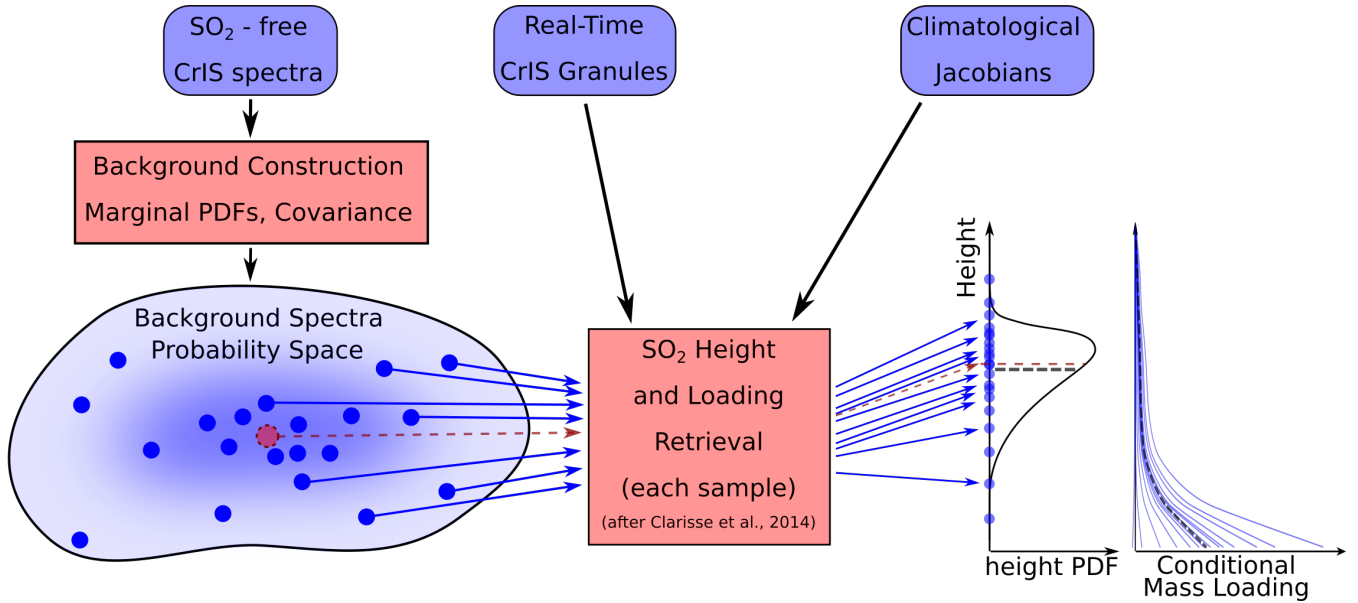
Figure 1. : *Flowchart showing probabilistic framework for Monte Carlo height and loading retrieval, yielding a PDF for the height which is not generally Gaussian and may even be skewed and a Gaussian distribution of conditional mass loading ($\hat{X}|H{=}h$). The height retrieval of Clarisse et al. (2014) is shown schematically in red lines, giving a single height estimate which is not in general the mean height (approximately the black dotted line in the height PDF).*

150   We impose a Gaussian prior with mean and variance given by MC sampling using the model columns that make up the Jacobian with noise added. Specifically, we use the Jacobian corresponding to the traditional Clarisse et al. (2014) height retrieval (h_C). The appropriate zero-mean noise is generated by $\mathbf{Y}-\mathbb{E}[\mathbf{Y}]$ and the model spectral anomaly is $\mathbf{F}\big[\epsilon\delta(h-h_C);\mathbf{u}\big]-\mathbf{F}\big[0;\mathbf{u}\big]=\epsilon\mathbf{K}(h_C)$. The mean and variance can therefore be expressed as

$$\begin{cases}\mu_H^{prior} = \mathbb{E}[g(\epsilon\mathbf{K}(h_C),\mathbf{Y}-\mathbb{E}[\mathbf{Y}])] & \text{(14a)}\\ (\sigma_H^{prior})^2 = \mathrm{Var}[g(\epsilon\mathbf{K}(h_C),\mathbf{Y}-\mathbb{E}[\mathbf{Y}])]. & \text{(14b)}\end{cases}$$

155   These values are similar to Fig. 2 of Clarisse et al. (2014), although they are calculated for each column to accommodate the spatial variation of the background. With the prior Gaussian distribution (f_H^{prior}) parameterized by μ_H^{prior} and σ_H^{prior}, our estimate of the height distribution is

$$f_H(h) \propto \mathcal{L}(h;\mathbf{y})f_H^{prior}(h) \tag{15}$$

where the proportionality is eliminated by normalizing the posterior PDF such that the total probability is unity.

160   Although slower than retrieving the layer height (h_C) due to a mean spectrum alone, this distribution provides significantly more information including the full PDF of H. This PDF may be used to calculate the maximum likelihood, expected value,

or median value of the retrieved height or probabilities of finding the plume in a given altitude interval. Additionally, this PDF is essential for calculating the mass loading correctly according to probability theory as detailed in the following section.

2.3 Probabilistic Mass Loading

165 Although this method is used primarily for detection (using z-scores) and height estimation, it is also used to estimate the mass loading, which we treat here as a random variable $\hat{X}$. Because the total column depends strongly on the layer height, we calculate the conditional loading random variable after Walker et al. (2011, 2012):

$$\hat{X}|H{=}h \; = \; \cos\theta\,[\mathbf{K}^{\intercal}(h)\mathbf{S}^{-1}\mathbf{K}(h)]^{-1}\mathbf{K}^{\intercal}(h)\mathbf{S}^{-1}(\mathbf{y} - \mathbf{Y}) \tag{16}$$

where an air mass factor equal to the cosine of the satellite zenith angle ($\cos\theta$) has been applied. This formula is in some
170 sense a probabilistic enhancement of an optimal unconstrained least-squares mass loading estimate. Similar to the z-scores, this function is normally distributed at every height with mean $\mathbb{E}[\hat{X} \mid H{=}h]$ and variance $\mathrm{Var}[\hat{X} \mid H{=}h]$. In practice, these are calculated by the same MC sampling used to generate the height samples. The conditional loading is a random function of height which generally reflects the principles of the Beer-Lambert Law for any given realization. If the height of the SO_2 layer were known exactly, this function could be queried and the loading could be estimated. However, since the height of the
175 layer is known only probabilistically, that is as measured by the PDF $f_H(h)$, additional computation is required to determine the loading.

Although we do not know the vertical profile of SO_2 concentration, the retrieval assumptions involve the thin layer representation of the SO_2 as a Dirac delta. The total column is then

$$\hat{X} = \int\limits_{0}^{\infty} \hat{X}\delta(h - H)\,\mathrm{d}h \tag{17}$$

180 which does not depend upon the height. More generally, the cumulative mass loading below a certain altitude h is:

$$\hat{X}(h) = \int\limits_{0}^{h} \hat{X}\delta(\eta - H)\,\mathrm{d}\eta \tag{18}$$

which is zero for $h < H$ and equals $\hat{X}$ for $h > H$. Because the concentration profile is linear in the loading and the conditional loading calculated above is normally distributed, we take the loading to be normally distributed, thus requiring only two parameters: the mean and variance which can be found using the conditional loading function calculated above. In this study,
185 integration is performed numerically over a discretely sampled height domain. Sketches of the proofs for the mean, variance, and covariance formulae below are detailed in Appendix B.

The mean loading is found by the law of total expectation:

$$\mu_{\hat{X}}(h) := \mathbb{E}[\hat{X}(h)] = \int\limits_{0}^{h} f_H(\eta)\,\mathbb{E}[\hat{X} \mid H{=}\eta]\,\mathrm{d}\eta \tag{19}$$

where the expectation of the conditional loading is taken as the mean of the samples.

190   The variance can also be calculated from the statistics of the conditional loading expectation:

$$\sigma_{\hat{X}}^2(h) := \text{Var}[\hat{X}(h)] = \int_0^h f_H(\eta) \left[\text{Var}[\hat{X} \mid H{=}\eta] + \left(\mathbb{E}[\hat{X} \mid H{=}\eta]\right)^2 \right] d\eta - \mu_{\hat{X}}^2(h) \tag{20}$$

where $\text{Var}[\hat{X} \mid H{=}h]$ and $\mathbb{E}(\hat{X} \mid H{=}h)$ were previously estimated by MC sampling.

The covariance between cumulative mass loading up to two altitudes $h = a$ and $h = b$ with $b \geq a$ is

$$\Sigma_{\hat{X}}(a,b) := \text{Cov}[\hat{X}(a), \hat{X}(b)] = \sigma_{\hat{X}}^2(a) - \mu_{\hat{X}}(a)\left(\mu_{\hat{X}}(b) - \mu_{\hat{X}}(a)\right) \tag{21}$$

195   which is always less than $\text{Var}[\hat{X}(a)]$ unless $a = b$ since the loading is cumulative, yielding larger values at higher altitudes.

Of particular importance, these formulae may be used to calculate the expectation and variance values of the mass loading between two altitudes. The expected value is

$$\mathbb{E}[\hat{X}(b) - \hat{X}(a)] = \mu_{\hat{X}}(b) - \mu_{\hat{X}}(a). \tag{22}$$

and the variance for this loading is

200    $$\text{Var}[\hat{X}(b) - \hat{X}(a)] = \sigma_{\hat{X}}^2(b) + \sigma_{\hat{X}}^2(a) - \Sigma_{\hat{X}}(a,b) = \sigma_{\hat{X}}^2(b) + \mu_{\hat{X}}(a)\left(\mu_{\hat{X}}(b) - \mu_{\hat{X}}(a)\right). \tag{23}$$

In this system, we retrieve probabilistic SO_2 information in two stages. In the first stage we perform an initial detection using the classical method (Eq. 5) to pre-screen each CrIS field of view (FOV) that likely contains SO_2, taken as an initial maximum z-score greater than 5, that is, $z(h_C; \mathbf{y}, \overline{\mathbf{y}}) > 5$ (Walker et al., 2011, 2012; Clarisse et al., 2014). In the second stage, we retrieve the height PDF and the mean and variance cumulative loading functions of height for each CrIS FOV that satisfies this initial
205   z-score threshold. In both stages, the background spectrum and covariance are interpolated spatially at the CrIS FOV center location by a bilinear interpolation scheme using the four nearest grid cells (Appendix C).

2.4   Specialized Retrieval for Strong Loading

For strong SO_2 columns, which we define here heuristically as $z > 200$, an alternate retrieval is needed to increase sensitivity to large loading. This is clear from examination of the chosen formula for approximating the Jacobian (Eqn. 4) in which
210   the background state ($\hat{x}$) is zero DU and the perturbation (ϵ) is 5 DU. For strong loading, the sensitivity of the Jacobians to additional SO_2 is greatly reduced for most CrIS channels, so linearized Jacobians with only a 5 DU anomaly will drastically under predict the loading for a given brightness temperature difference (Fig. 2b). In order to construct a Jacobian that is more sensitive at higher mass loading values, the Jacobian must be dominated by channels with approximately linear responses (Fig. 2b). These channels were determined by constructing Jacobians with various anomaly strengths and choosing those channels
215   for which the Jacobians are approximately constant over anomaly strength. This channel subset (Appendix D) is used with the original 5 DU Jacobian which can be extrapolated successfully to high loading values because of the approximately linear model. From (Fig. 2) it is clear that the channels with the most linear response are also those which are least sensitive to
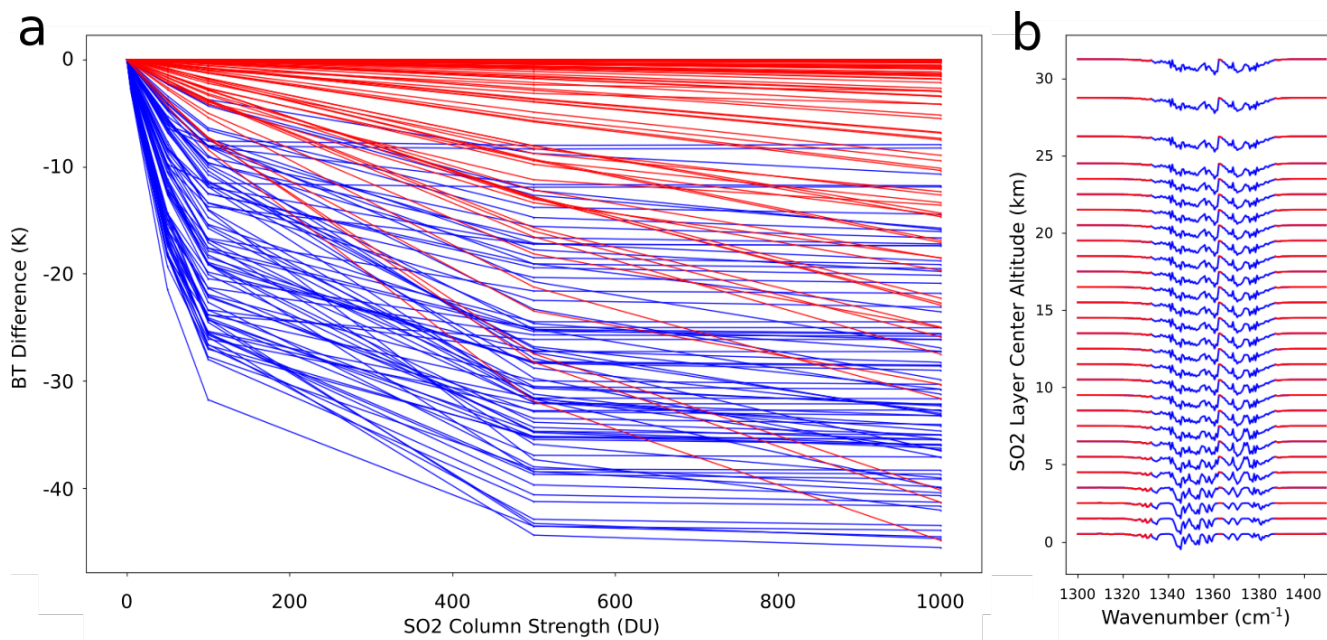
Figure 2. : *a) Channel-wise brightness temperature difference response to increasing mass loading. All channels here are used in the original retrieval. Red channels are used in the high loading retrieval due to their mostly linear response across the full range of reasonable mass loading. b) Height dependent Jacobians (normalized) showing specialized channel selection in (a).*

SO_2 loading. However, by applying this new retrieval only when strong loading ($z > 200$) is detected by the original retrieval, nontrivial brightness temperature differences are guaranteed. In theory, a sequence of increasingly restricted retrievals could be implemented to increase the sensitivity to even stronger loading values, such a study is beyond the scope of the present work.

2.5 Background State Construction

At every stage of the retrieval, the background state of the volcanic SO_2-free atmosphere must be accurate in order for this linearized method to succeed. Consequently, calculating accurate statistics of the background state is paramount. The CrIS instrument collects almost 3 million spectra per day, allowing for robust characterization of the background spectrum including variation across seasons and locations.

In constructing the background spectrum PDFs and covariance matrix, the periods with little or no SO_2 must be determined. We utilize the detailed record of global volcanic SO_2 emissions from the IASI SO_2 retrieval algorithm (L. Clarisse, *pers. comm.*) between 1 November, 2017 and 1 November, 2018, collecting all spectra measured on days with maximum total columns less than 1 DU SO_2 present anywhere in the atmosphere (Fig. 3a).

This omission leaves more than 3.6×10^8 SO_2-free spectra collected by CrIS over the one year period. We classify the spectra regionally and seasonally, partitioning the data into four seasons and $5° \times 5°$ latitude and longitude grid cells yielding 10,368 bins (Fig. 4), each of which has a full set of PDFs for each channel and a covariance matrix characterizing the correlation
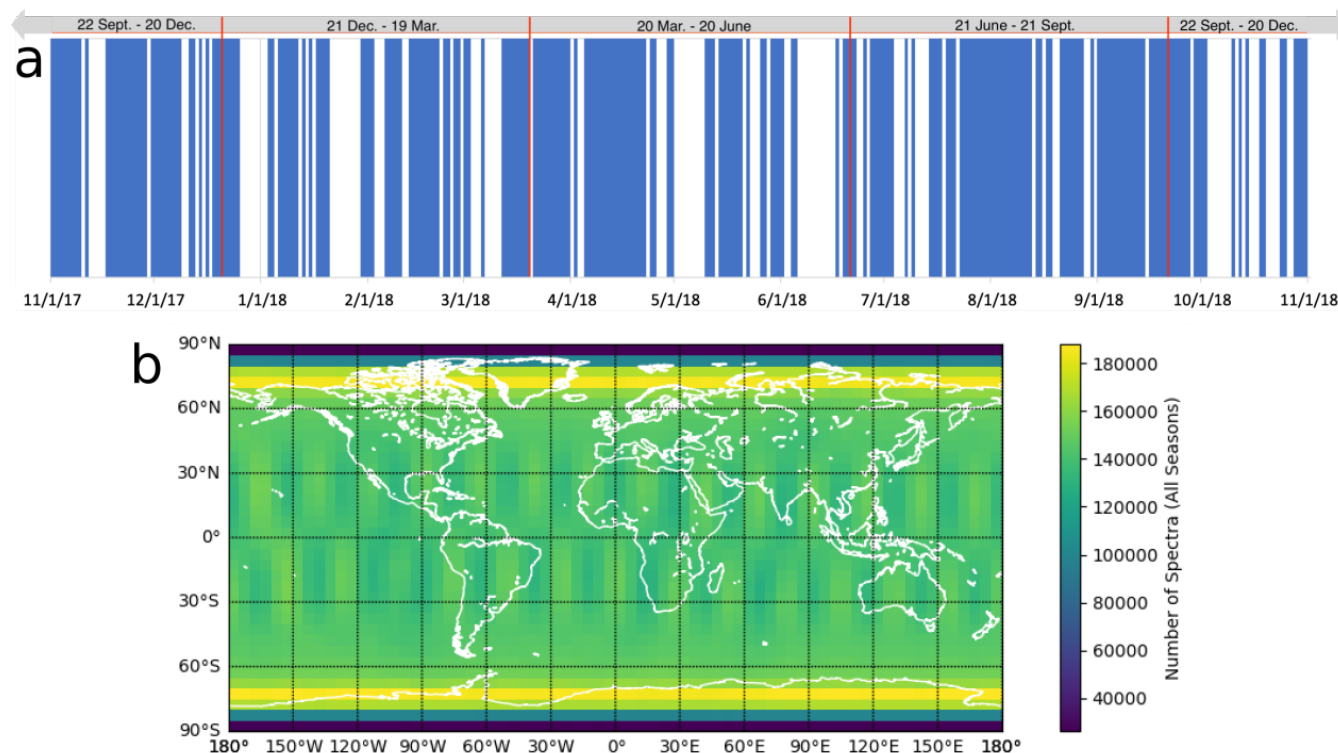
Figure 3. : *a) IASI-derived days with (blue) and without (white) SO_2 columns ≥ 1 DU in the one year background construction interval (1 Nov. 2017 - 1 Nov., 2018). Date intervals across top define seasons. b) Histogram showing the number of S-NPP CrIS spectra in each latitude, longitude cell totaled over the one year interval.*

structure among the channels. This partitioning reduces the the overall variability represented in the mean spectra and thus also reduces the magnitude of the error covariance matrix entries while still capturing the fundamental variability due to spectral
235 trends between regions and throughout a year.

3 Results

3.1 Test Case I: Raikoke, Kuril Islands, 2019

At approximately, 18:00 UTC on June 21, 2019 (4:00 AM local time), Raikoke volcano in the Kuril Islands erupted for the first time since 1924 (Sennert, 2019; Hedelt et al., 2019). The strongest pulses of the eruption rose to an altitude of approximately
240 13 km, forming an umbrella cloud which was quickly advected to the east by strong winds. In the first hours of the eruption, SO_2 columns of > 900 DU (Hedelt et al., 2019, >1000 DU, S. Carn, *pers. comm.*) were detected. The strongest individual measurement made by our method (48.52107 N, 167.25615 W, 15:22:25 UTC, 22 June, 2019) had a mean total column of 432 DU with standard deviation total column of 15 DU (Fig. 5); however, because there is significantly greater uncertainty within
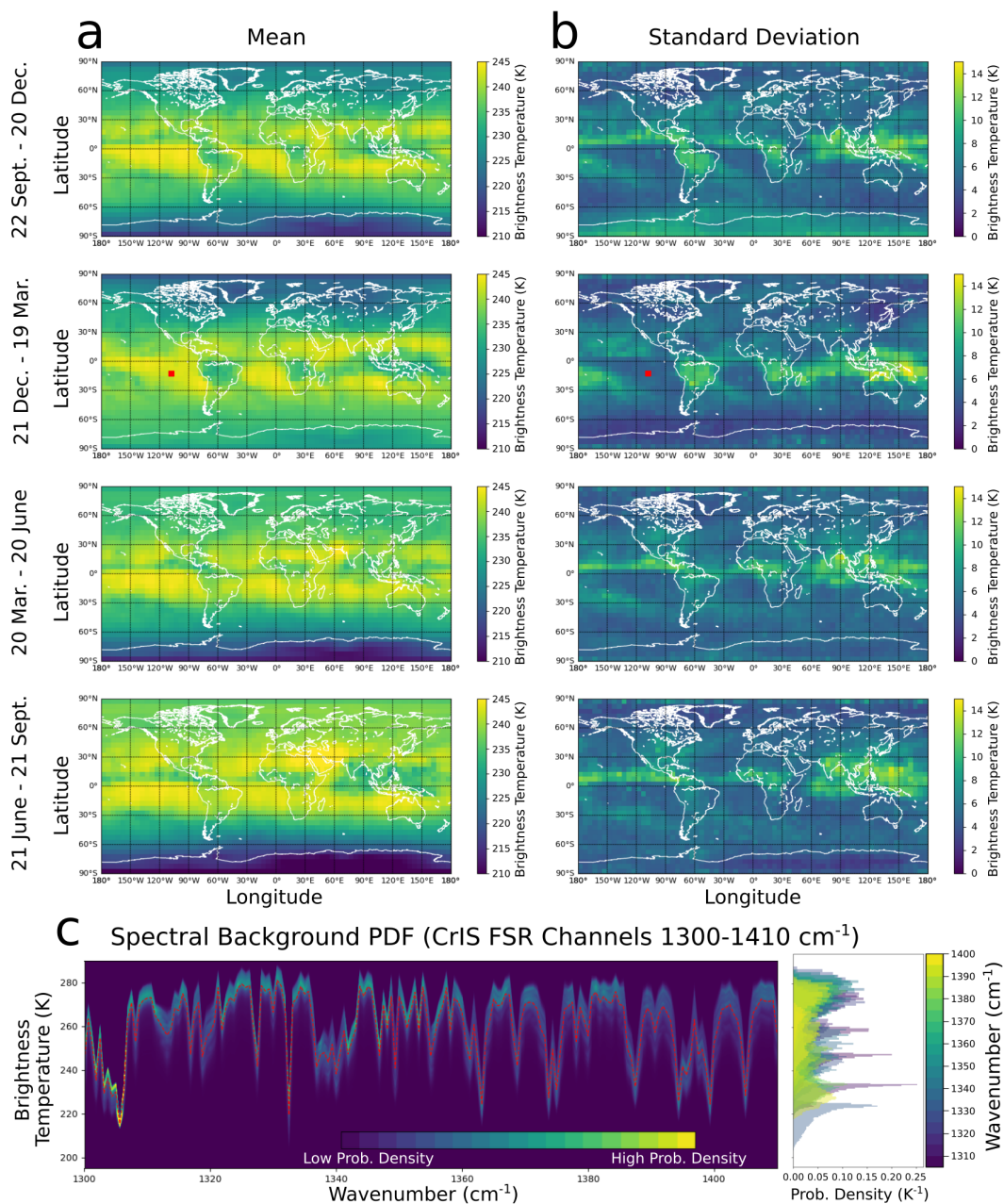
Figure 4. : *S-NPP CrIS mean (a) and standard deviation (b) brightness temperature at $1300\ cm^{-1}$ for each grid cell and each season interval. The red grid cell corresponds to the data shown in (c). c) Marginal PDF of the background spectrum indicated by the red cell in (a,b) with mean spectrum (red dashes) and several individual marginal PDFs (right) shown.*

the support of the height PDF, the largest value of mean plus uncertainty occurs just below the upper end of the height PDF
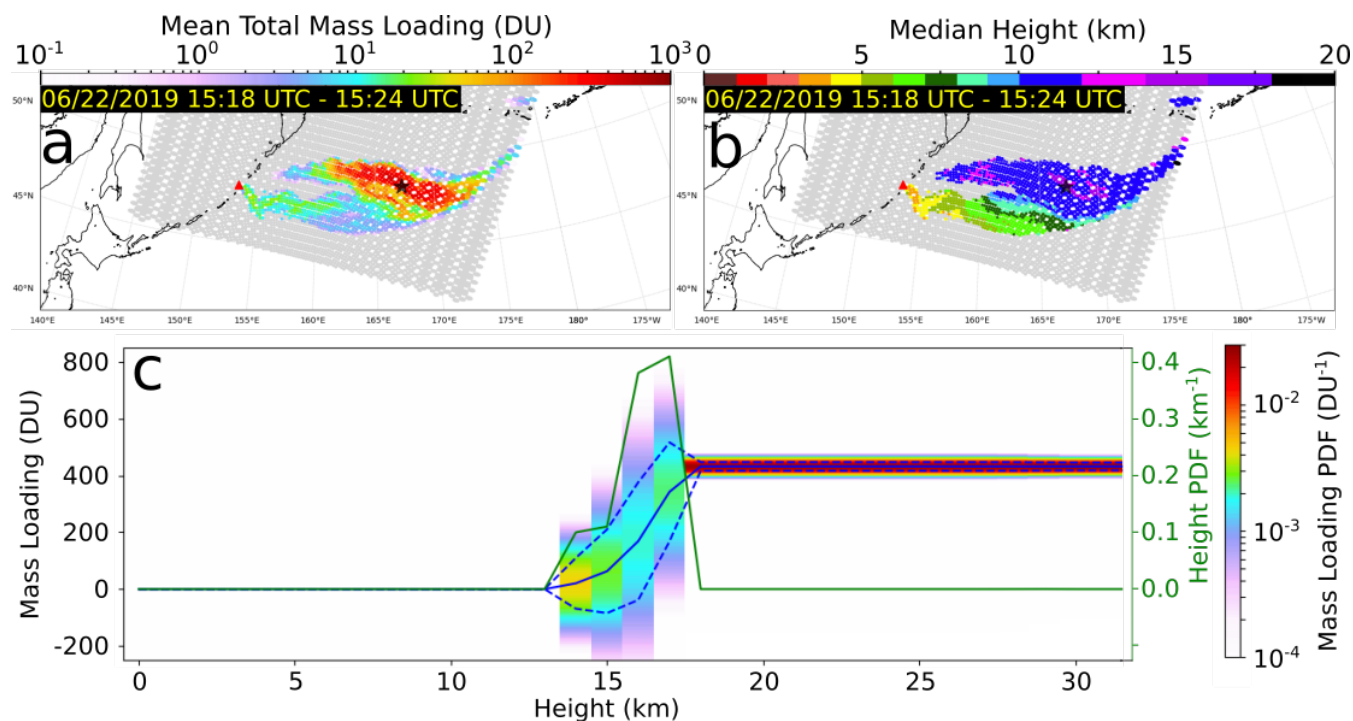
Figure 5. : *NOAA-20 CrIS mean total mass loading (a) and median height (b) early in the evolution of the Raikoke eruption cloud. Star indicates location of (c). c) Probabilistic retrieval of* SO_2 *layer altitude (PDF, green) and cumulative mass loading (mean, blue solid; mean ± standard deviation, blue dotted; PDF, colorbar) for the strongest individual total column measured by CrIS in the Raikoke cloud (48.52107 N, 167.25615 W, 22 June, 2019, 15:22:25 UTC).*

245 support (Fig. 5c). This underestimate early in the Raikoke cloud history was likely due two factors, channel saturation despite the specialized strong column retrieval and the fact that the footprint of the CrIS FOVs leaves many gaps where extremal values could have been present. As described above, more specialized retrievals could be devised to increase the sensitivity to very strong loading as in the Raikoke case; however, such schemes are beyond the scope of this work, which is principally concerned with advances in height information. Within about one day, the ash and SO_2 were entrained into a large extratropical

250 cyclone which heavily distorted the dispersion of the cloud, with the SO_2 cloud being pushed to the north and dispersing in both easterly and westerly directions (Fig. 6). Early in this complex dispersion, SO_2 columns remained strong despite a rapid decline in eruptive output. This is most likely a result of the convergence caused by entrainment into the cyclone. Based on the probabilistic retrieval and tropopause data from the National Centers for Environmental Prediction (NCEP), it is clear that the vast majority of the SO_2 cloud mass was in the lower stratosphere, with only a small lower layer in the mid-upper troposphere

255 which had mostly dispersed after the first week (Fig. 6b-l). After one month, the SO_2 cloud had spread out over most of the northern hemisphere above 30° N with most columns < 2 DU; however, some columns remained as strong as 20 DU. After two months, traces of the SO_2 cloud remained over Northern Canada and the Hudson Bay with columns up to 1 DU.
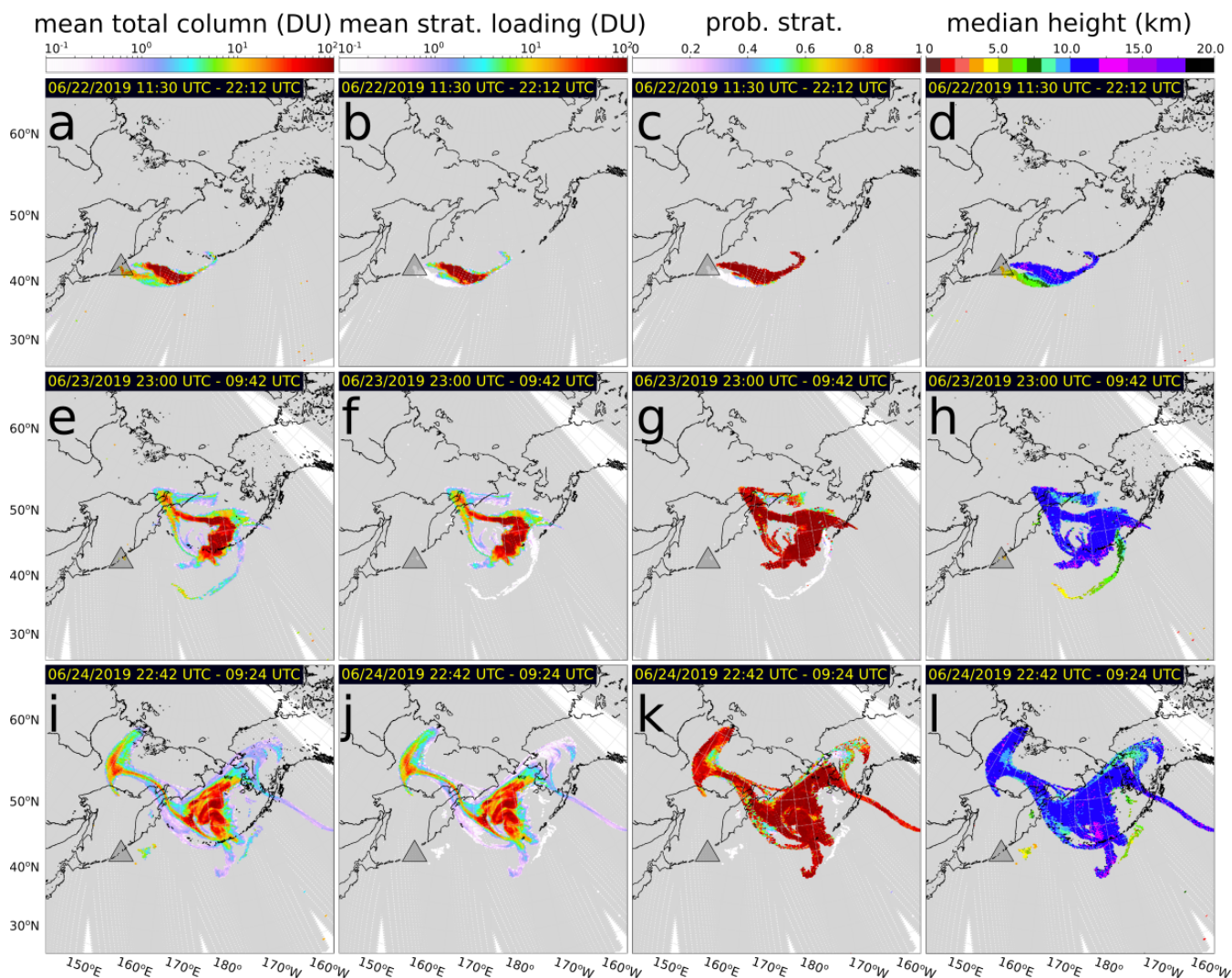
Figure 6. : *Time evolution (top to bottom) of the Raikoke* SO_2 *plume from NOAA-20 CrIS showing the expected value total column loading (a,e,i), the expected value stratospheric column loading (b,f,j), the probability that the* SO_2 *layer is in the stratosphere (c,g,k) and the median layer height (d,h,l). The height of the tropopause was calculated from daily NCEP reanalysis data.*

3.2 Test Case II: Early Detection of SO_2 Emission from Bogoslof Volcano, Aleutian Islands, 2016

In the 2016 - 2017 eruptive period at Bogoslof volcano, 70 explosive events were identified (Coombs et al., 2018, 2019). The first five explosions were not detected in real time, and could only be identified and characterized after reanalysis of satellite and other data sources (Coombs et al., 2019). The first CrIS detection of the SO_2 cloud from this sequence of explosions occurred at UTC 22:48 on 16 December, 2016 (approximately 300 km NE of Bogoslof), which was most likely the Event 4 (UTC 18:39) SO_2 plume drifting downwind (Coombs et al., 2018, 2019). As noted in Coombs et al. (2018), the USGS Alaska
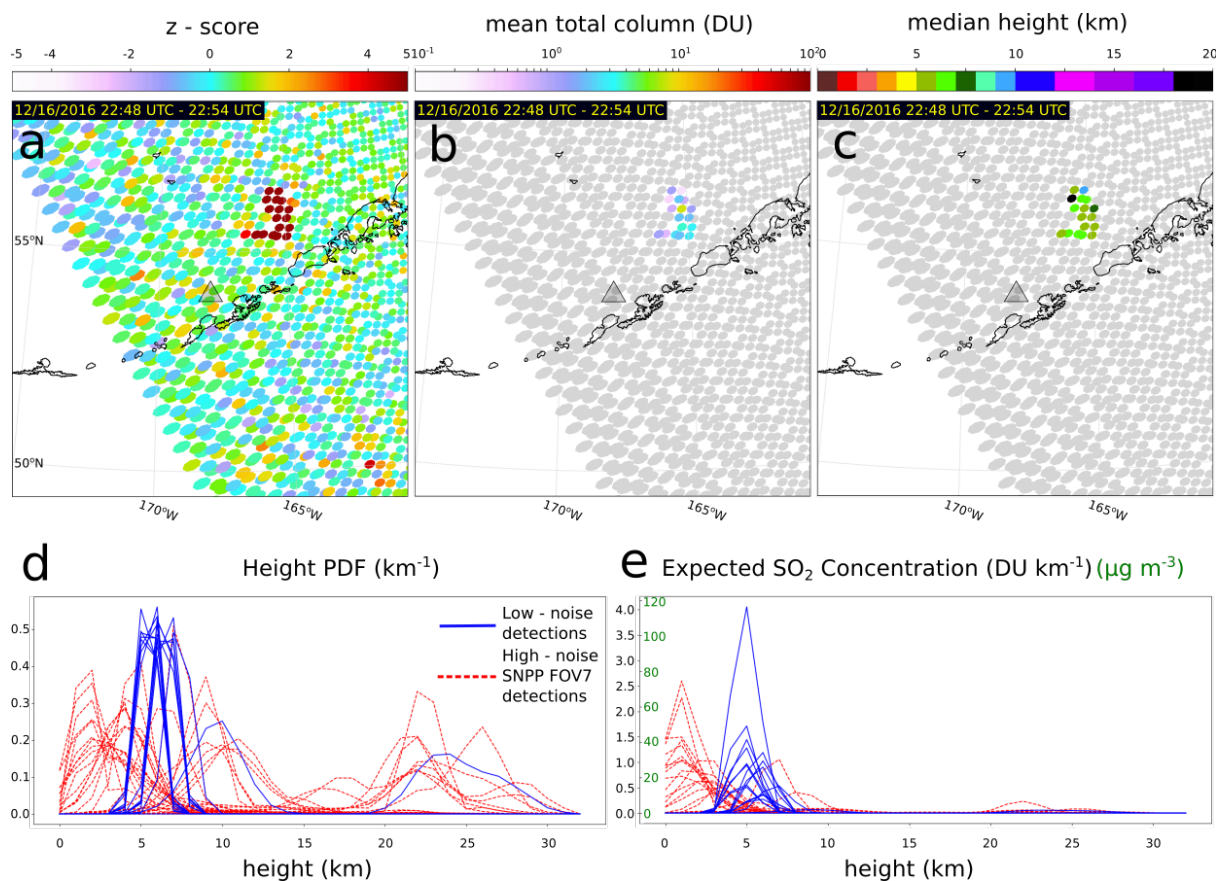
Figure 7. : *Upper: Initial (classical) z-score (a), mean total column (b), and median height (c) for an explosion from Bogoslof very early in the 2016 - 2017 eruption (S-NPP CrIS). Lower: Height PDFs (d) and expected (mean) cloud concentration (e), mean concentration profiles for the detected* SO_2 *cloud. Retrievals from the high noise S-NPP CrIS FOV 7 (red dotted in lower panel) are not shown in (a,b,c).*

Volcano Observatory (AVO) was not able to issue a Volcanic Activity Notice (VAN) for this event and consequently no height

265   information was generated until the reanalyses of Schneider et al. (2020) in which a cloud height of 6.1 km was determined. This small pulse was not observable by the multispectral infrared remote sensing methods nor by automated analysis of multispectral signatures and cloud growth rates (Pavolonis et al., 2013, 2015a, b, 2018; Schneider et al., 2020). The CrIS estimated heights are mainly clustered between 5 - 8 km with some scatter due to localized cloud edge effects (Fig. 7c,d). This is broadly consistent with the reanalysis of Schneider et al. (2020).

270   Of particular importance in this small cloud made up of only a few CrIS FOVs, the midwave IR for FOV 7 on the CrIS instrument aboard S-NPP is significantly nosier (above specification) than that of other FOVs (Zavyalov et al., 2013; Han et al., 2013) and consequently, the FOV 7 retrievals are highly suspect and have been omitted (Fig. 7). Because the probabilistic framework allows the calculation of a mean cumulative mass loading, we may derive a formula for the mean or expected

concentration profile by similar means as for Eq. 19:

$$275 \quad \mathbb{E}[C(h)] = \mathbb{E}[\frac{d}{dh}\hat{X}(h)] = f_H(h)\,\mathbb{E}[\hat{X} \mid H{=}h] \tag{24}$$

which is shown for FOVs in the detected Bogoslof cloud (Fig. 7e). This example demonstrates that the CrIS SO_2 detection and characterization scheme is sufficiently sensitive to capture some small emissions which are generally difficult to observe by other means.

3.3 Test Case III: Resolving Strong Stratification in an SO_2 Plume, Sierra Negra, Galapagos Islands, 2018

280 On 26 June, 2018 after a period of elevated seismicity, the onset of a major eruption at Sierra Negra was signaled by volcanic tremor at 19:40 UTC, producing an ash and SO_2 plume at 20:09 UTC (Carn et al., 2018; Vasconez et al., 2018; Hedelt et al., 2019). The first CrIS observation also occurred at 20:09 UTC from S-NPP, detecting SO_2 above the Sierra Negra on 3 adjacent FOVs on the edge of scan with maximum initial z-scores of approximately 9, 16, and 31. Subsequent overpasses show the plume rising to approximately 14 - 19 km and spreading in a complex manner due to vertical wind shear as evidenced by the
285 lower plume altitudes spreading towards the west and the upper plume altitudes spreading towards the southeast (Fig. 8). The significant shearing of the eruption column enables observations of the cloud at many levels. Consequently, this eruption forms a good opportunity to highlight the broad sensitivity of this method in detecting and characterizing SO_2 at every elevation from the vent (1.124 masl) up to $\sim$14 - 19 km and potentially higher. Additionally, this example highlights the strength of the probabilistic height retrieval, enabling the retrieval of any desired confidence interval on the height. Here we compute the
290 90% confidence interval (Fig. 8), highlighting the fact that the 95th- and 5th- percentile are not in general symmetric about the median nor are the same size at different locations within the plume. Because our method retrieves consistent statistics across all measurements, we can ensure the stability of the method and derived probabilities in particular, giving good smoothness even without post-processing. As described above this is not necessarily the case for other height retrievals which compute a single estimate with constant uncertainty.

295 ## 4 Discussion

4.1 Comparison with other data

Although a deep analysis of the differences between the present method and others is beyond the scope of the present work, here we highlight a brief, representative comparison of our SO_2 retrievals with data from TROPOMI, IASI, and CALIOP during the evolution of the Raikoke eruption cloud.
300 As mentioned above, our strongest total column loading from the Raikoke cloud was 432 DU. This is significantly lower than the maximum detected by TROPOMI (> 900 DU, (Hedelt et al., 2019)), and several other UV-based methods ($\sim$1000 DU, S. Carn, *pers. comm.*). This suggests that our method, despite the integrated height estimate and the specialized retrieval for strong loading, currently cannot fully capture extremely high column loading values; however, away from these extreme values, our retrieval performs well in comparison to TROPOMI and IASI (Fig. 9 a-e). Other than the relatively few columns
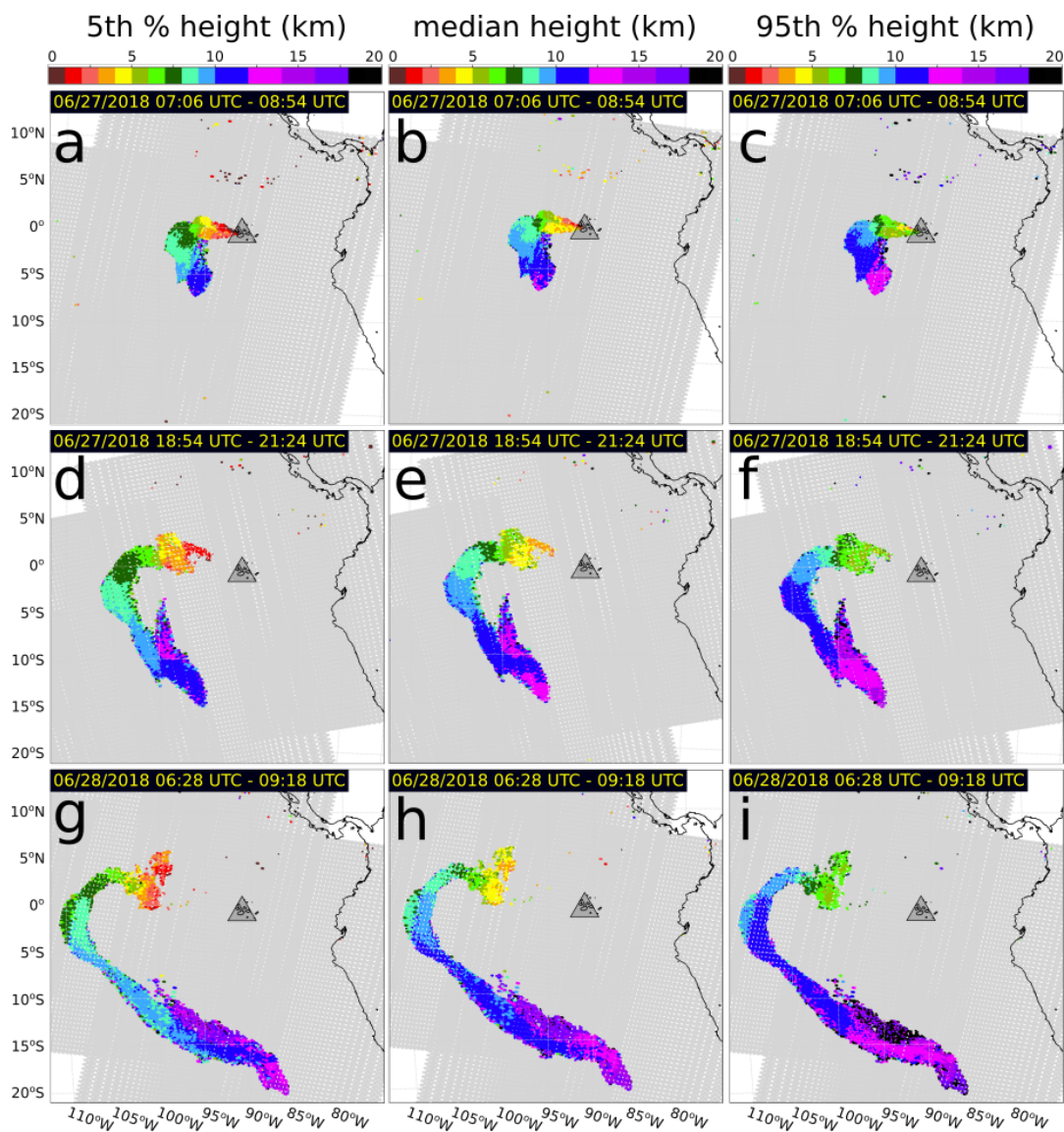
Figure 8. : *Time evolution (top to bottom) of the 27 June, 2018 Sierra Negra* SO_2 *plume height represented as the 5th-percentile (a,d,g), median (b,e,h), and 95th-percentile (c,f,i) heights. Data is merged S-NPP CrIS and NOAA-20 CrIS with S-NPP CrIS FOV 7 excluded.*

305   with unusually large loading, the largest discrepancy between the TROPOMI-retrieved Raikoke cloud and that from CrIS is that the CrIS retrieval does not resolve the smaller diffuse cloud to the south of the main cloud, although the CrIS retrieval does resolve some similar features elsewhere in the cloud. This may be due to the very high spatial resolution of the TROPOMI data (7×3.5 km^2 pixels at nadir) compared with the coarse CrIS resolution (~ 154 km^2 FOVs at nadir with gaps between FOVs). An additional contributing factor is that the CrIS retrieval starts with an initial detection of the z-score (Fig. 9 j) and
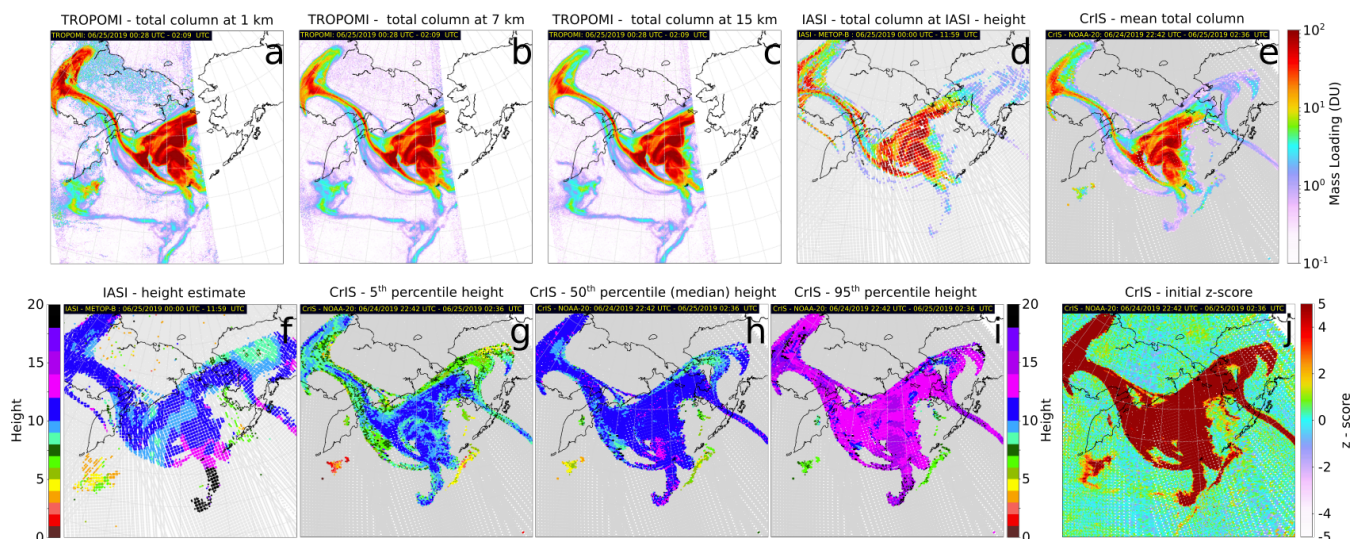
Figure 9. : *Representative comparison between TROPOMI, IASI, and CrIS SO₂ data. Top: TROPOMI total column loading given a 1 km-thick layer at 1 km (a), 7 km (b), and 15 km (c) altitudes; IASI (METOP-B) total column given a 1 km-thick layer at the IASI height estimate (f); and CrIS (NOAA-20) mean total column loading (integrated against the height PDF). Bottom: IASI height estimate (f); CrIS 5th(g)-, 50th(median, h)-, and 95th(i)- percentile heights; CrIS initial z-score (j).*

310 only retrieves the height and loading for FOVs with $z > 5$. Evidence for this smaller diffuse cloud are present in the initial z-score field, although it mostly presents with a z-score below this threshold. Lastly, this discrepancy may also be due to spectral interference from water vapor in the CrIS SO₂ infrared band (1300 - 1410 cm^{-1}), although our approach is generally insensitive to the presence of background levels of water vapor by construction.

The strength of our approach lies in our ability to generate physics-based PDFs for the height. Because our height retrieval is
315 based on the operational algorithm in use for IASI, our retrieved heights are very similar to those from IASI although there are key differences. As mentioned above, the IASI heights represent the height retrieved due to the mean background spectrum; however, because the retrieval of height is not necessarily linear (due to the $\arg\max$ function), the retrieved height is not the expected value height. Inspection of the PDFs generated by this approach show that they are typically non-symmetric, meaning that IASI heights are also not necessarily the maximum likelihood estimated heights, although exact comparison is
320 not possible due the orbital separation between the satellites carrying IASI (METOP-A,B) and those carrying CrIS (S-NPP, NOAA-20). Because of this mathematical point, the IASI heights also cannot be said to represent a consistent metric or statistic of the height, meaning that there may be significant inconsistency between measurements. At least for the Raikoke cloud, the IASI heights are almost entirely bound within the CrIS 90% confidence interval (Fig. 9 f,g,i) and are very similar to the CrIS median heights (Fig. 9 h). For the snapshot of the Raikoke cloud shown in Fig. 9, the largest differences in height appear at
325 the southernmost part of the cloud, where the IASI heights are > 19 km altitude over a significant region. Furthermore, the

IASI height estimate (Fig. 9 f) varies significantly over nearby, continuous parts of the cloud, whereas the CrIS median height is more consistent across space with some minor variation due to noise.

Although not shown here, Hedelt et al. (2019) have recently developed a new SO$_2$ height retrieval for TROPOMI using inverse learning machines. Although computationally expensive to train, such an approach has the advantage of computation speed of the inversion once deployed, though it has not yet been incorporated into the TROPOMI SO2 data product as of this writing, so a direct comparison is not possible. However, it is clear from the data presented in Hedelt et al. (2019) that their height estimates for the Raikoke cloud span the CrIS 90% confidence interval, though they are significantly nosier than CrIS SO$_2$ height estimates and display a very prominent negative trend in height versus total column loading, leading to systematically higher layer heights on the cloud edges than in the cloud centers (Fig. 14 of Hedelt et al., 2019). The CrIS PDFs do not show this trend.

Because we retrieve a PDF on each CrIS FOV rather than a single estimate, we can compare the PDFs directly to CALIOP data as CALIPSO passes over the cloud. Here we show an example comparison from Raikoke; however, a full comparison for every overpass of the Raikoke cloud is the subject of future work. For the first several days after the eruption, there was still significant ash suspended in the dispersing cloud, leading to the appearance of several highly attenuating layers in CALIOP data between 10 - 15 km (Fig. 10 a,b). The comparison we focus on is between CrIS retrievals from 14:18:00 - 14:24:00 UTC and CALIOP data from a subsequent overpass between 14:32:06 - 14:36:14 UTC on 25 June, 2019. To make the comparison as exact as possible, the CrIS FOVs are first interpolated to fill space and then sampled at the points given by the CALIPSO overpass, creating a profile of the CrIS PDFs. Overall, there is good agreement between the CrIS SO$_2$ PDFs and the altitudes of the strongly attenuating CALIOP layers; however, the CrIS PDFs have several important characteristics that complicate comparison. There is some minor noise derived mainly from two CrIS FOVs at the cloud edge ($\sim 175°$ W), exactly at the CALIPSO track, leading to unrealistically high altitudes there (Fig. 10 e). Most obviously, some regions of the cloud have bimodal PDFs which may have several interpretations (Fig. 10 b,c). The CrIS retrieval assigns significant probability mass to the same locations as the strongly attenuating layers, suggesting that they are at least a mix of ash, SO$_2$ and sulfate aerosols. Where this cloud rises up to 14 - 15 km, the CrIS retrieval also assigns significant probability mass to a lower layer between 11 - 13 km (Fig. 10 b,c). This may indicate the presence of a separate molecular SO$_2$ layer at this altitude. Indeed, this part of the CALIOP layer is very strongly attenuating and may completely shadow any evidence of a lower weakly attenuating sulfate aerosol layer. However, this lower layer may merely be a (true) probability artifact inherited from the background spectrum probability space. If the background spectrum has multiple modes (for example, one mode representing deep convective cloud radiances and another for cloud-free radiances), then multiple populations of the Monte-Carlo height samples may accumulate, leading to a multimodal height PDF.

4.2   Long-term analysis of the Raikoke SO$_2$ cloud

By retrieving PDFs for height and cumulative mass loading it is possible to enhance time series analysis of SO$_2$ clouds accordingly, enabling the generation of time series with quantified uncertainty. As an example, we calculate the total and stratospheric SO$_2$ mass time series probabilistically as sums of many independent retrievals (Fig. 11).
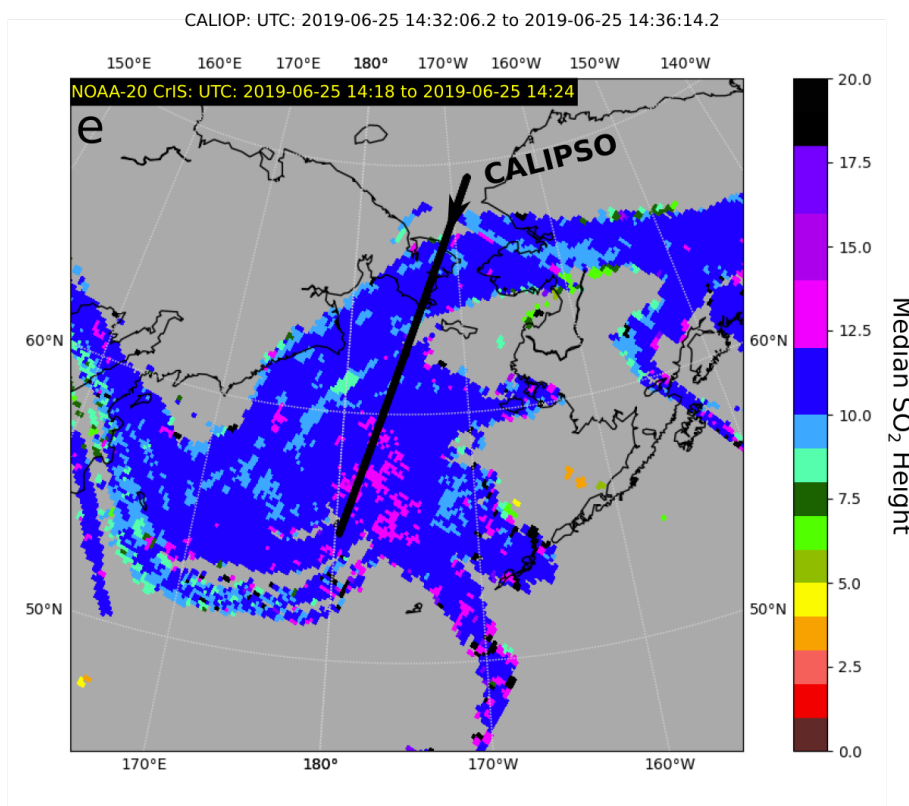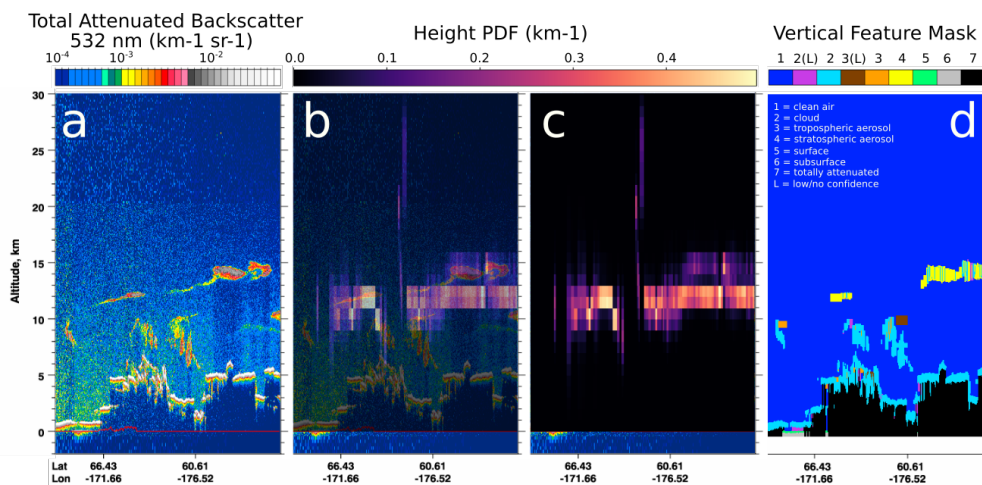
Figure 10. : *Representative example comparison of CALIOP lidar backscatter (a, b), CrIS SO₂ height PDFs (b-transparent, c), and CALIOP vertical feature mask (d) for the Raikoke cloud on 25 June, 2019. e) Nearest neighbor gridded interpolation of CrIS SO₂ median heights with closest CALIPSO overpass shown (black, arrow indicating descending orbit, < 15 minutes after CrIS acquisition).*
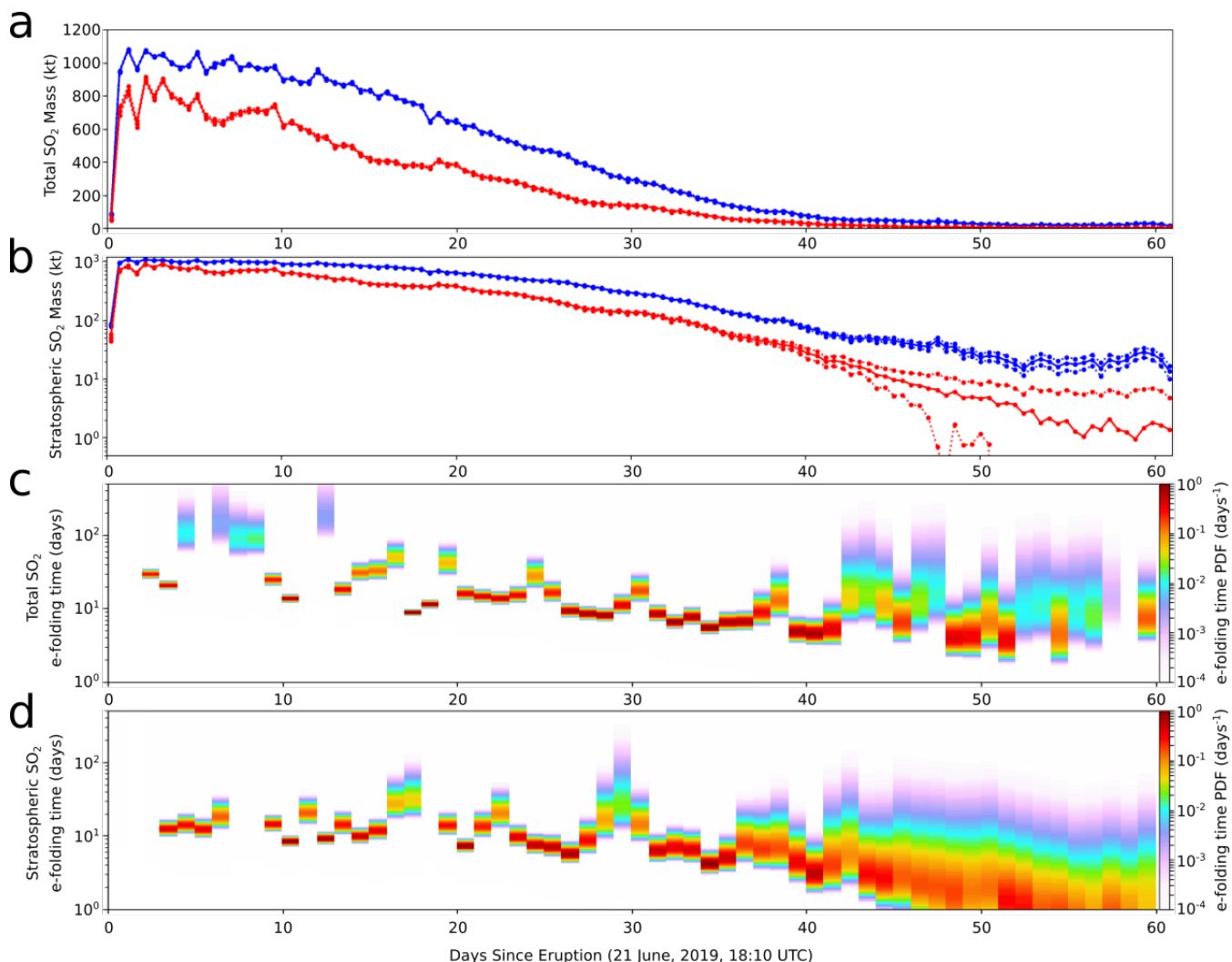
Figure 11. : *a) Total (blue) and stratospheric (red) mass of* SO_2 *above 30° N for two months following the eruption of Raikoke showing CrIS-derived mean (solid lines) ± 1 standard deviation (dotted lines). b) Log-scale copy of (a). "Instantaneous" (daily-aggregated) e-folding time PDFs for the total (c) and stratospheric (d)* SO_2 *in the Raikoke eruption cloud.*

360   To estimate the mass of an SO_2 cloud, the values of the retrieval on the CrIS FOVs must be interpolated onto a continuous grid spanning the cloud. In the present study we use an equal-area grid with area element δA and perform nearest neighbor interpolation of the CrIS FOV retrievals. Consequently we calculate the total cloud mass in units of kilotons (kt) of SO_2 as a Riemann sum:

$$M \approx \kappa \delta A \sum_i \hat{X}_i(h_\infty) \tag{25}$$

365 where $\kappa = 2.8617 \times 10^{-11}$ kt m^{-2} DU^{-1} and the $\hat{X}_i(h_\infty)$ are the gridded cumulative mass loading values at the top of the atmosphere h_∞. By aggregating enough CrIS FOVs to completely cover the area of a cloud, a total cloud mass can be approximated. Furthermore, because the loading measurements are independent random variables, the total cloud mass is a normal random variable and the mean and variance of the cloud mass are:

$$
\begin{cases}
\mathbb{E}(M) = \kappa \delta A \sum_i \mathbb{E}[\hat{X}_i(h_\infty)] & \text{(26a)} \\
\mathrm{Var}(M) = (\kappa \delta A)^2 \sum_i \mathrm{Var}[\hat{X}_i(h_\infty)]. & \text{(26b)}
\end{cases}
$$

The mass of SO$_2$ in the stratosphere can be calculated similarly if the height of the tropopause h_{trop} is available from

370 ancillary data sources. The mass loading in the stratosphere is $\hat{X}_{strat} = \hat{X}(h_\infty) - \hat{X}(h_{trop})$ which is a normal random variable independent from all other locations. By analogy to the total cloud mass calculation, the mean and variance of the stratospheric cloud mass are therefore:

$$
\begin{cases}
\mathbb{E}(M_{strat}) = \kappa \delta A \sum_i \mathbb{E}[\hat{X}_i(h_\infty) - \hat{X}_i(h_{trop})] & \text{(27a)} \\
\mathrm{Var}(M_{strat}) = (\kappa \delta A)^2 \sum_i \mathrm{Var}[\hat{X}_i(h_\infty) - \hat{X}_i(h_{trop})]. & \text{(27b)}
\end{cases}
$$

where the mean and variance of $\hat{X}_{strat}$ are calculated as in (Eqns. 22 and 23).

Additionally, we compute from these results the "instantaneous" e-folding time of the SO$_2$ as $\tau = -M(t)/\dot{M}(t)$ with $\dot{M}(t)$

375 calculated by finite difference and the PDFs computed by standard results in probability theory (Fieller, 1932; Hinkley, 1969; DeGroot and Schervish, 2012, Appendix E).

From Fig. 11 it is clear that the SO$_2$ cloud, as characterized by CrIS, did not immediately show the exponential mass decay that has been used in similar studies of large eruptions (e.g., Read et al., 1993; Carn et al., 2017; Krotkov et al., 2010). The observed trend is likely a combination of retrieval limitations and genuine atmospheric chemical properties. As described

380 above, the CrIS SO$_2$ loading strength underestimate early in the Raikoke cloud history was likely due to channel saturation despite the specialized strong column retrieval. The strongest CrIS total columns were only approximately 50% of the strongest columns reported at the time; 432 DU from CrIS vs. >900 DU (Hedelt et al., 2019) and >1000 DU (S. Carn *pers. comm.*). Such strong columns did not persist for many overpasses; however, total SO2 mass did not begin an exponential decay until approximately 20 days after SO$_2$ injection, suggesting that in the first several weeks, the reaction kinetics, and consequently

385 the e-folding time, were strongly varying. This could have been the result of limited hydroxyl radical (OH) early in the cloud history (e.g., Theys et al., 2013; Sekiya et al., 2016). As the e-folding times shown in Fig. 11c,d are calculated by finite difference, they are quite noisy; however, they exhibit the same trend of slow decay early in the cloud history, settling into a constant decay rate later ($\sim$10 day e-folding time). The large uncertainty in the stratospheric e-folding time after approximately 40 days is the result of the mean mass decaying below the order of magnitude of the standard deviation mass and the particular

390 details of the PDF calculation (Hinkley, 1969).

5   Conclusions

i) New probabilistic enhancement of existing hyperspectral IR SO_2 retrieval techniques enable the retrieval of PDFs for SO_2 height and cumulative mass loading, providing significant statistical power, precision, and consistency to global SO_2 detection, tracking, and forecasting efforts. Retrieving these PDFs enables the calculation of many new quantities, including

395   exceedence probabilities for concentration, layer height constraint probabilities, mean concentration profiles, and mass at different layers with uncertainty. Although these capabilities are primarily beneficial for operational SO_2 monitoring, these methods are relevant to climatological studies because of the ability to calculate PDFs for the stratospheric fraction of total mass of a given SO_2 cloud where the tropopause height is available from ancillary sources.

ii) This technique is capable of resolving strong SO_2 mass loading based on a specialized retrieval with less sensitive CrIS

400   channels; however, it is limited in its ability to resolve extreme mass loading values like some of those observed in the recent eruption of Raikoke Volcano, Kuril Islands. Because of the improved spatial resolution over IASI and the technique's sensitivity, we can resolve small clouds that are undetectable by other means. Additionally, the technique can adequately resolve height information across a broad range of plume altitudes including the lower stratosphere.

iii) Preliminary comparisons suggest that this method compares well with other measurements of SO_2 mass loading and

405   altitude; however, the probabilistic framework adds significant value over these techniques especially in the retrieval of height information. Cross sections through these probability clouds compare very well with cloud heights from CALIOP lidar backscatter.

iv) This technique enables the probabilistic characterization of SO_2 clouds for long-term analysis of cloud evolution and key time-varying parameters such as total mass, stratospheric mass, and e-folding time.

410   v) The algorithms presented here are currently being integrated into VOLCAT, where they will be used for operational SO_2 cloud detection, characterization, and tracking in support of aviation safety. We anticipate future work to include more comprehensive comparison of height PDFs with CALIOP lidar backscatter data, applyication of these techniques to similar instruments including IASI and the Atmospheric Infrared Sounder (AIRS), development of volcanic degassing and aviation-focused products, and analysis of errors in the trace gas technique induced by a warming background atmosphere.

415   *Code and data availability.* The Level - 1B CrIS data utilized in this study are available from the Goddard Earth Sciences Data and Information Services Center (GES-DISC, https://disc.gsfc.nasa.gov/). The tropopause data used here to define the lower limit of the stratosphere are available from the NOAA Earth Science Research Laboratory (ESRL, https://www.esrl.noaa.gov/psd/data/gridded/ data.ncep.reanalysis.html) The code developed to generate samples of the SO_2-free background spectrum by the NORTA process are available in a git repository at https://gitlab.ssec.wisc.edu/dhyman/trace_gas_background_spectra. This repository also includes a list of the SO_2-free days discussed in the

420   text as well as GES-DISC links for all of the CrIS granules collected during those days.

Appendix A: Generating Correlated Random Spectra for Monte Carlo Retrieval: NORTA Sampling

The general problem of sampling a correlated random vector ($Y_i \in \mathbf{Y} \in \mathbb{R}^N$) with non-normal marginal distributions F_{Y_i} and covariance matrix $\mathbf{S}$ is accomplished by a transform sampling technique known as NORTA (NORmal To Anything) (Cario and Nelson, 1997) in which the desired random vector is written as a component-wise inverse marginal transform of a standard normal random vector:

$$Y_i = F_{Y_i}^{-1}(\Phi(Z_i)) \tag{A1}$$

where Φ is the univariate standard normal CDF. In this formulation, the individual marginals can be used to transform the components of the standard normal vector. The crux of this method lies in generating a standard normal random vector $\mathbf{Z}$ with appropriate correlation structure $\rho_\mathbf{Z}$ which upon component-wise transformation as above, will produce the desired random vector $\mathbf{Y}$ with the desired covariance structure $\mathbf{S}$. That is, a correlated $\mathbf{Z}$ must be generated with the correlation matrix

$$\rho_\mathbf{Z} = \mathrm{Cov}(\mathbf{Z}) = \mathbb{E}\left[\mathbf{Z}\mathbf{Z}^\mathsf{T}\right], \tag{A2}$$

which, after transformation, results in the correlation matrix $\rho_\mathbf{Y} = \mathrm{Corr}(\mathbf{Y})$ associated with the the known covariance matrix $\mathbf{S}$.

This is accomplished by solving

$$\rho_\mathbf{Y}(i,j) = C_{ij}\left[\rho_\mathbf{Z}(i,j)\right] \tag{A3}$$

for each of the unique $N(N-1)/2$ correlations ($\rho_\mathbf{Z}(i,j)$) in the lower triangle of $\rho_\mathbf{Z}$. The correlation transformation function is

$$C_{ij}\left[\rho_\mathbf{Z}(i,j)\right] := \frac{\mathbb{E}[Y_i(Z_i)Y_j(Z_j)] - \mathbb{E}[Y_i]\mathbb{E}[Yj]}{\sqrt{\mathrm{Var}[Y_i]\mathrm{Var}[Y_i]}} \tag{A4}$$

and

$$\mathbb{E}[Y_i(Z_i)Y_j(Z_i)] = I\left[\rho_\mathbf{Z}(i,j)\right] := \iint\limits_{\mathbb{R}^2} F_{Y_i}^{-1}[\Phi(z_i)]F_{Y_j}^{-1}[\Phi(z_j)]\varphi(z_i, z_j; \rho_\mathbf{Z}(i,j))\,\mathrm{d}z_i\,\mathrm{d}z_j \tag{A5}$$

where $\varphi(z_i, z_j; \rho_\mathbf{Z}(i,j))$ is the bivariate standard normal density function with correlation $\rho_\mathbf{Z}(i,j)$ between the variables Z_i and Z_j. These problems may be inverted individually by various methods outlined in the original formulation of Cario and Nelson (1997).

A1 Application of NORTA to background spectrum

For the purposed of generating the correlated random background spectrum in the present study, we make several modifications to the classical method of Cario and Nelson (1997) to make our problem tractable but retain the high fidelity of the CrIS measurements. In the present study, 177 CrIS channels are used representing the FSR mid-wave band between $1300 - 1410$ cm^{-1}. This yields $15,576$ independent correlation - matching inverse problems which are solved in the present study by gradient descent iteration.

A2 Numerical Integration of the Joint Expectation

Because each of the correlation - matching inverse problems requires multiple rounds of numerical integration of Eqn. A5, we make several modifications to increase computational efficiency. Because many of the channel correlations are strong, the bivariate standard normal distribution $\varphi(z_i, z_j; \rho_{\mathbf{Z}}(i,j))$ for each such pair of channels is very narrow. Consequently, for a typical rectangular sampling domain, the integrand of Eqn. A5 is approximately zero almost everywhere except for a concentrated region in which accurate numerical integration is challenging. To reduce wasted integrand samples, we make a standard transformation of the bivariate normal distribution and then cast the domain in polar coordinates and approximate the integral over a finite radial domain $[0, R]$:

$$I[\rho] := \int_0^{2\pi} \int_0^R G_{ij}(r,\theta;\rho) \frac{e^{-r^2/2}}{2\pi} r \, \mathrm{d}r \, \mathrm{d}\theta \tag{A6}$$

where

$$G_{ij}(r,\theta;\rho) = F_{Y_i}^{-1}[\Phi(r\cos\theta)] \, F_{Y_j}^{-1}[\Phi(\rho r\cos\theta + \sqrt{1-\rho^2} \, r\sin\theta)] \tag{A7}$$

is the product of the transformed i-th and j-th components of the desired random vector. This approximates the full improper integral within tolerance ϵ, with the fixed value $\epsilon = 10^{-6}$ in the present study. The terminal radius is estimated conservatively as

$$R = \sqrt{2\ln\left(\frac{1}{\epsilon} \frac{\max Y_i \max Y_j}{\min Y_i \min Y_j}\right)} \tag{A8}$$

where the maximum and minimum values of the components were recorded during the generation of $\mathbf{S}$ and the marginal distributions from sample data. In the absence of knowledge of these minima and maxima, they could be estimated from the marginal distributions as fixed percentiles of these distributions.

The estimated radial limit of integration R is derived by requiring that

$$\int_0^{2\pi} \int_R^\infty G_{ij}(r,\theta;\rho) \frac{e^{-r^2/2}}{2\pi} r \, \mathrm{d}r \, \mathrm{d}\theta \le \epsilon \int_0^{2\pi} \int_0^\infty G_{ij}(r,\theta;\rho) \frac{e^{-r^2/2}}{2\pi} r \, \mathrm{d}r \, \mathrm{d}\theta. \tag{A9}$$

This inequality can be solved for R under the conservative estimation that $\max G_{ij} = \max Y_i \max Y_j$ and $\min G_{ij} = \min Y_i \min Y_j$ which are finite in this case due to the collection of a finite number of spectra for the generation of the channel marginals. This leads to

$$\int_R^\infty r e^{-r^2/2} \, \mathrm{d}r \le \epsilon \frac{\min Y_i \min Y_j}{\max Y_i \max Y_j} \int_0^\infty r e^{-r^2/2} \, \mathrm{d}r \tag{A10}$$

and upon integrating, R may be chosen conservatively to satisfy

$$e^{-R^2/2} \le \epsilon \frac{\min Y_i \min Y_j}{\max Y_i \max Y_j}. \tag{A11}$$

This transformation to a scaled polar coordinates ensures that the curvature and gradients in the integrand are as small as possible, ensuring that numerical integration is as accurate as possible for a given domain sampling up to the order of the method employed. Additionally, the sensible radial limitation of this integral ensures that it can be computed efficiently to within tolerance without the inclusion of samples which minimally affect the total (approximately Gaussian tails).

480 ## A3   Numerical Solution of Inverse Problems

Although each channel pair inverse problem can be solved separately by Newton's method or other algorithms, we solve all of the problems jointly, restating the problem as a gradient - descent minimization of the total square correlation error

$$\varepsilon^2(\mathbf{r_Z}) = \left[\mathbf{C}(\mathbf{r_Z}) - \mathbf{r_Y} \right]^\mathsf{T} \left[\mathbf{C}(\mathbf{r_Z}) - \mathbf{r_Y} \right], \tag{A12}$$

where the vectors $\mathbf{r_Z}, \mathbf{r_Y} \in \mathbb{R}^{15,576}$ are comprised of the unique lower triangular elements of ρ_Z and ρ_Y respectively and
485 $\mathbf{C} : \mathbb{R}^{15,576} \to \mathbb{R}^{15,576}$ is the correlation transformation function cast as a vector function. Although this seems intractable due to the extreme dimensionality, there is no correlation between these dimensions (no correlation between pairwise inverse problems), and consequently, the Jacobian is zero everywhere except for its main diagonal. The gradient descent method of Barzilai and Borwein (1988) produces fast convergence to a global minimum due to the monotonicity and bounding properties of the correlation functions C_{ij} as described by Cario and Nelson (1997). At each iteration, the NORTA processes is completed
490 and the error on the synthesized channel marginal distributions and spectral covariance matrix are used as convergence criteria. The vectorization of these independent problems allows for standardization in convergence criteria using global (total) error minimization. Because the error is measured on the final product (the desired random spectra), a minimum number of iterations is required by comparison with performing each problem separately and then generating the desired random spectra.

Appendix B: Proof of mass loading mean, variance, and covariance formulae

495 The calculation of the mean and variance make extensive use of Fubini's Theorem allowing reordering of iterated integration. Because these integrals contain the Dirac delta, it is not simple to show that the conditions of Fubini's theorem are satisfied due to the Lebesgue non-integrability of the Dirac delta, which in turn stems from the fact that the Dirac delta is not a function, but a distribution. However, we proceed assuming that the iterated integrals can be interchanged. We remark that a proof using limits of functions ("nascent delta functions") approaching the Dirac delta could be substituted here at great cost to simplicity
500 and readability. If a finite thickness layer must be used, then all convolutions with the Dirac delta below are replaced with convolution with a nascent delta function and the convolutions will result in filtered or local-averaged quantities. For example, if a rectangular nascent delta is used, the results of convolution will be smoothed, local-averaged version of the desired function. The final integral formulas will be expressed in terms of integrals of these filtered functions.

The mean cumulative mass loading is calculated as the expectation

505

$$\mathbb{E}[\hat{X}(h)] = \mathbb{E}\left[\int_0^h \hat{X}\delta(\eta - H)\,\mathrm{d}\eta\right] = \int_{\mathcal{H}}\int_{\mathcal{X}}\left(\int_0^h \hat{x}\delta(\eta - h')\,\mathrm{d}\eta\right)f_{\hat{X},H}(\hat{x},h')\,\mathrm{d}\hat{x}\,\mathrm{d}h'$$

$$= \int_{\mathcal{H}}\int_{\mathcal{X}}\left(\int_0^h \hat{x}\delta(\eta - h')\,\mathrm{d}\eta\right)f_{\hat{X}\,|\,H}(\hat{x}\,|\,h')f_H(h')\,\mathrm{d}\hat{x}\,\mathrm{d}h' \quad \text{(B1)}$$

where $\mathcal{H}$ and $\mathcal{X}$ are the domains of height and loading (both σ-finite measure spaces) and the last equality follows from the definition of the conditional probability density. Rearranging this iterated integral gives

510

$$\mathbb{E}[\hat{X}(h)] = \int_0^h\int_{\mathcal{H}}\delta(\eta - h')f_H(h')\left(\int_{\mathcal{X}}\hat{x}f_{\hat{X}\,|\,H}(\hat{x}\,|\,h')\,\mathrm{d}\hat{x}\right)\mathrm{d}h'\,\mathrm{d}\eta$$

$$= \int_0^h\int_{\mathcal{H}}\delta(\eta - h')\,f_H(h')\,\mathbb{E}(\hat{X}\,|\,H = h')\,\mathrm{d}h'\,\mathrm{d}\eta. \quad \text{(B2)}$$

Because of the symmetry of the delta function ($\delta(\eta - h') = \delta(h' - \eta)$), the integral properties of the delta function yields

$$\mathbb{E}[\hat{X}(h)] = \int_0^h f_H(\eta)\,\mathbb{E}(\hat{X}\,|\,H = \eta)\,\mathrm{d}\eta. \quad \text{(B3)}$$

515   Because the algebraic form of the variance is $\mathrm{Var}(\hat{X}(h)) = \mathbb{E}[\hat{X}^2(h)] - [\mathbb{E}(\hat{X}(h))]^2$, only the second moment of the cumulative loading $\mathbb{E}[\hat{X}^2(h)]$ must be calculated to complete the formula. This quantity is

$$\mathbb{E}[\hat{X}^2(h)] = \mathbb{E}\left[\left(\int_0^h \hat{X}\delta(\eta - H)\,\mathrm{d}\eta\right)^2\right]$$

$$= \int_{\mathcal{H}}\int_{\mathcal{X}}\left(\int_0^h \hat{x}\delta(\eta_0 - h')\,\mathrm{d}\eta_0\right)\left(\int_0^h \hat{x}\delta(\eta - h')\,\mathrm{d}\eta\right)f_{\hat{X}\,|\,H}(\hat{x}\,|\,h')f_H(h')\,\mathrm{d}\hat{x}\,\mathrm{d}h'$$

520

$$= \int_0^h\int_0^h\int_{\mathcal{H}}\delta(\eta_0 - h')\delta(\eta - h')f_H(h')\left(\int_{\mathcal{X}}\hat{x}^2 f_{\hat{X}\,|\,H}(\hat{x}\,|\,h')\,\mathrm{d}\hat{x}\right)\mathrm{d}h'\,\mathrm{d}\eta_0\,\mathrm{d}\eta$$

$$= \int_0^h\int_0^h\int_{\mathcal{H}}\delta(h' - \eta_0)\delta(h' - \eta)f_H(h')\,\mathbb{E}(\hat{X}^2\,|\,H = h')\,\mathrm{d}h'\,\mathrm{d}\eta_0\,\mathrm{d}\eta$$

$$= \int_0^h\int_0^h\delta(\eta_0 - \eta)f_H(\eta_0)\,\mathbb{E}(\hat{X}^2\,|\,H = \eta_0)\,\mathrm{d}\eta_0\,\mathrm{d}\eta$$

(B4)

Since the dummy variable η always runs between $0 < \eta < h$, the delta function $\delta(\eta_0 - \eta)$ is always centered in the interval

525    $0 < \eta_0 < h$ and the integral properties of the delta function can be applied again:

$$\mathbb{E}[\hat{X}^2(h)] = \int_0^h f_H(\eta)\,\mathbb{E}(\hat{X}^2 \,|\, H = \eta)\,\mathrm{d}\eta. \tag{B5}$$

Substitution of $\mathbb{E}(\hat{X}^2 \,|\, H = \eta) = \mathrm{Var}(\hat{X} \,|\, H = \eta) + [\mathbb{E}(\hat{X} \,|\, H = \eta)]^2$ into the formula for $\mathbb{E}[\hat{X}^2(h)]$ and subsequently into the

formula above for $\mathrm{Var}(\hat{X}(h))$ completes the proof of the variance.

Similarly, for the covariance between cumulative mass loading up to two altitudes $h = a$ and $h = b$ with $b \geq a$, only the

530   mixed expectation $\mathbb{E}[\hat{X}(b)\hat{X}(a)]$ must be calculated:

$$\mathbb{E}[\hat{X}(a)\hat{X}(b)] = \mathbb{E}\left[\int_0^a \hat{X}\delta(\eta_a - H)\,\mathrm{d}\eta_a \int_0^b \hat{X}\delta(\eta_b - H)\,\mathrm{d}\eta_b \right]$$

$$= \int_{\mathcal{H}}\int_{\mathcal{X}} \left(\int_0^a \hat{x}\delta(\eta_a - h')\,\mathrm{d}\eta_a \right)\left(\int_0^b \hat{x}\delta(\eta_b - h')\,\mathrm{d}\eta_b \right) f_{\hat{X}\,|\,H}(\hat{x}\,|\,h')f_H(h')\,\mathrm{d}\hat{x}\,\mathrm{d}h'$$

$$= \int_0^a \int_0^b \int_{\mathcal{H}} \delta(h' - \eta_b)\delta(h' - \eta_a)f_H(h')\,\mathbb{E}(\hat{X}^2 \,|\, H = h')\,\mathrm{d}h'\,\mathrm{d}\eta_b\,\mathrm{d}\eta_a. \tag{B6}$$

535   because the domains $(0, a)$, $(0, b)$, and $\mathcal{H}$ have the relationship

$$(0, a) \subseteq (0, b) \subseteq \mathcal{H}, \tag{B7}$$

it follows that $\eta_a \in \mathcal{H}$, $\eta_b \in \mathcal{H}$, and $0 < \eta_a < \eta_b$, so that

$$\mathbb{E}[\hat{X}(a)\hat{X}(b)] = \int_0^a \int_0^b \delta(\eta_b - \eta_a)f_H(\eta_b)\,\mathbb{E}(\hat{X}^2 \,|\, H = \eta_b)\,\mathrm{d}\eta_b\,\mathrm{d}\eta_a$$

540    $$= \int_0^a f_H(\eta_a)\,\mathbb{E}(\hat{X}^2 \,|\, H = \eta_a)\,\mathrm{d}\eta_a = \mathbb{E}[\hat{X}^2(a)]. \tag{B8}$$

Using the algebraic formula for the variance and covariance, we attain by substitution

$$\mathrm{Cov}[\hat{X}(a), \hat{X}(b)] = \mathrm{Var}[\hat{X}(a)] - \mathbb{E}[\hat{X}(a)]\Big(\mathbb{E}[\hat{X}(b)] - \mathbb{E}[\hat{X}(a)] \Big) \tag{B9}$$

which is always less than $\mathrm{Var}[\hat{X}(a)]$ unless $a = b$ since the loading is cumulative, yielding larger values at higher altitudes.

Remark:

545   Of particular importance, these formula may be used to calculate the expectation and variance values of the mass loading

between two altitudes. The expected value is

$$\mathbb{E}[\hat{X}(b) - \hat{X}(a)] = \mathbb{E}[\hat{X}(b)] - \mathbb{E}[\hat{X}(a)]. \tag{B10}$$

and the variance is

$$\mathrm{Var}[\hat{X}(b) - \hat{X}(a)] = \mathrm{Var}[\hat{X}(b)] + \mathrm{Var}[\hat{X}(a)] - \mathrm{Cov}[\hat{X}(a), \hat{X}(b)]$$

$$= \mathrm{Var}[\hat{X}(b)] + \mathbb{E}[\hat{X}(a)]\Big(\mathbb{E}[\hat{X}(b)] - \mathbb{E}[\hat{X}(a)]\Big). \quad \text{(B11)}$$

Appendix C: Bilinear interpolation of background spectrum

To smooth the changes between retrievals in adjacent background cells, we use a bilinear interpolation of the background spectra. For a general quantity (Q), the bilinear interpolation is represented as

$$Q(x,y) = c_x c_y Q(x_0, y_0) + (1 - c_x) c_y Q(x_1, y_0) + c_x (1 - c_y) Q(x_0, y_1) + (1 - c_x)(1 - c_y) Q(x_1, y_1) \quad \text{(C1)}$$

between the corner points (x_0, y_0), (x_1, y_0), (x_0, y_1), (x_1, y_1), using the scalings $c_x = (x_1 - x)/(x_1 - x_0)$ and $c_y = (y_1 - y)/(y_1 - y_0)$. We interpolate the inverse error covariance matrix $\mathbf{S}^{-1}$ by this formula. However, because our background spectrum is characterized probabilistically as a set of $N = 10,000$ samples ($\mathbf{y}^s \in \Omega_{\mathbf{Y}}$) of a correlated random vector $\mathbf{Y}$ in each seasonal $5° \times 5°$ background grid cell, the samples cannot be interpolated directly by the above formula. Instead we treat $\mathbf{Y} = \mathbf{Y}(X, Y)$ as a function of a random position where (X, Y) is a discrete random position, taking only the cell corner points as possible values. In this case, X and Y represent longitude and latitude. In particular, we characterize (X, Y) by the probability mass function $p(x_i, y_j) = (-1)^{i+j}(i - c_x)(j - c_y)$ for $i, j \in \{0, 1\}$ which is simply the corner point weights in the bilinear interpolation formula. Consequently, we generate $\mathbf{Y}(x, y) = \mathbb{E}_{(X,Y)}[\mathbf{Y}(X, Y)] = \sum_{i,j} \mathbf{Y}(x_i, y_j) p(x_i, y_j)$ by sampling the discrete distribution $p(x_i, y_j)$ to generate the number of samples taken from each of the corner points $n(x_i, y_j) = [Np(x_i, y_j)]$ where the bracket represents rounding to the nearest integer. Using this sampling, we generate the samples of $\mathbf{Y}(x, y)$ as the collection of each of the $n(x_i, y_j)$ samples from the corners $\mathbf{Y}(x_i, y_j)$. This generates a total of N samples for the interpolated background spectrum.

Appendix D: CrIS Channels used in SO2 retrieval

The following CrIS channels are used in this work and are identified by their wavenumber value (cm^{-1}).

D1   For the regular retrieval:

1300.0 , 1300.625, 1301.25 , 1301.875, 1302.5 , 1303.125, 1303.75 , 1304.375, 1305. , 1305.625, 1306.25 , 1306.875, 1307.5 , 1308.125, 1308.75 , 1309.375, 1310. , 1310.625, 1311.25 , 1311.875, 1312.5 , 1313.125, 1313.75 , 1314.375, 1315. , 1315.625, 1316.25 , 1316.875, 1317.5 , 1318.125, 1318.75 , 1319.375, 1320. , 1320.625, 1321.25 , 1321.875, 1322.5 , 1323.125, 1323.75 , 1324.375, 1325. , 1325.625, 1326.25 , 1326.875, 1327.5 , 1328.125, 1328.75 , 1329.375, 1330. , 1330.625, 1331.25 , 1331.875, 1332.5 , 1333.125, 1333.75 , 1334.375, 1335. , 1335.625, 1336.25 , 1336.875, 1337.5 , 1338.125, 1338.75 , 1339.375, 1340. , 1340.625, 1341.25 , 1341.875, 1342.5 , 1343.125, 1343.75 , 1344.375, 1345. , 1345.625, 1346.25 , 1346.875, 1347.5 ,

1348.125, 1348.75 , 1349.375, 1350. , 1350.625, 1351.25 , 1351.875, 1352.5 , 1353.125, 1353.75 , 1354.375, 1355. , 1355.625, 1356.25 , 1356.875, 1357.5 , 1358.125, 1358.75 , 1359.375, 1360. , 1360.625, 1361.25 , 1361.875, 1362.5 , 1363.125, 1363.75 , 1364.375, 1365. , 1365.625, 1366.25 , 1366.875, 1367.5 , 1368.125, 1368.75 , 1369.375, 1370. , 1370.625, 1371.25 , 1371.875,

580 1372.5 , 1373.125, 1373.75 , 1374.375, 1375. , 1375.625, 1376.25 , 1376.875, 1377.5 , 1378.125, 1378.75 , 1379.375, 1380. , 1380.625, 1381.25 , 1381.875, 1382.5 , 1383.125, 1383.75 , 1384.375, 1385. , 1385.625, 1386.25 , 1386.875, 1387.5 , 1388.125, 1388.75 , 1389.375, 1390. , 1390.625, 1391.25 , 1391.875, 1392.5 , 1393.125, 1393.75 , 1394.375, 1395. , 1395.625, 1396.25 , 1396.875, 1397.5 , 1398.125, 1398.75 , 1399.375, 1400. , 1400.625, 1401.25 , 1401.875, 1402.5 , 1403.125, 1403.75 , 1404.375, 1405. , 1405.625, 1406.25 , 1406.875, 1407.5 , 1408.125, 1408.75 , 1409.375, 1410.0

585 **D2 For the specialized, high-loading retrieval:**

1300. , 1300.625, 1301.25 , 1301.875, 1302.5 , 1303.125, 1303.75 , 1304.375, 1305. , 1305.625, 1306.25 , 1306.875, 1307.5 , 1308.125, 1308.75 , 1309.375, 1310. , 1310.625, 1311.25 , 1311.875, 1312.5 , 1313.125, 1313.75 , 1314.375, 1315. , 1315.625, 1316.25 , 1316.875, 1317.5 , 1318.125, 1318.75 , 1319.375, 1320. , 1320.625, 1321.25 , 1321.875, 1322.5 , 1323.125, 1323.75 , 1324.375, 1325. , 1325.625, 1326.25 , 1326.875, 1327.5 , 1328.125, 1328.75 , 1329.375, 1330. , 1330.625, 1331.25 , 1331.875,

590 1332.5 , 1362.5 , 1363.125, 1363.75 , 1387.5 , 1388.125, 1388.75 , 1389.375, 1390. , 1390.625, 1391.25 , 1391.875, 1392.5 , 1393.125, 1393.75 , 1394.375, 1395. , 1395.625, 1396.25 , 1396.875, 1397.5 , 1398.125, 1398.75 , 1399.375, 1400. , 1400.625, 1401.25 , 1401.875, 1402.5 , 1403.125, 1403.75 , 1404.375, 1405. , 1405.625, 1406.25 , 1406.875, 1407.5 , 1408.125, 1408.75 , 1409.375, 1410.

Appendix E: Probabilistic time series

595 **E1 Probabilistic mass**

In general, the total cloud mass can be calculated be integrating the total columns $\hat{X}(h_\infty)$ over the SO$_2$ cloud region Ω:

$$M = \int_\Omega \hat{X}(h_\infty)\,\mathrm{d}A \tag{E1}$$

Where M has units of DU m^2. In practice this is calculated as a Riemann sum:

$$M \approx \kappa \sum_i \delta A_i\,\hat{X}_i(h_\infty) \tag{E2}$$

600 where M now has units of kilotons (kt) of SO$_2$ and the factor $\kappa = 2.8617 \times 10^{-11}$ kt m^{-2} DU^{-1} has been included for dimensional consistency with a total column measured in DU. In the present study, we make this calculation after interpolating the CrIS retrievals onto an equal area grid. Because the individual measurements are independent and normally distributed with means $\mathbb{E}[\hat{X}_i(h_\infty)]$ and variances $\mathrm{Var}[\hat{X}_i(h_\infty)]$, their sum is also normally distributed (DeGroot and Schervish, 2012):

$$M \sim \mathcal{N}(\mathbb{E}(M), \mathrm{Var}(M)) \tag{E3}$$

where the mean is

$$\mathbb{E}(M) = \kappa\,\delta A \sum_i \mathbb{E}[\hat{X}_i(h_\infty)] \tag{E4}$$

and variance is

$$\mathrm{Var}(M) = (\kappa\,\delta A)^2 \sum_i \mathrm{Var}[\hat{X}_i(h_\infty)]. \tag{E5}$$

This given the total cloud mass as a PDF for any period of data coverage.

E2   Probabilistic decay rate coefficient and e-folding time

We treat the above time series of PDFs of SO_2 mass as a random process M_t. As a continuous process, the conversion of SO_2 into sulfur aerosols can be modelled kinetically by the differential equation $\dot{M}_t = -k_t M_t$ where k_t is the instantaneous decay rate coefficient. Below we generate k_t and the e-folding time $\tau_t = k_t^{-1}$ as random processes from M_t.

To make this calculation in practice, a finite difference formula is needed for $\dot{M}_t$. We write this as a general 2α - order accuracy central finite difference formula for the first derivative:

$$\dot{M}_t \approx \frac{1}{\delta t} \sum_{i=-\alpha}^{\alpha} \delta_{t+i} M_{t+i} \tag{E6}$$

where δ_{t+i} are the central difference scheme coefficients. As before, the weighted sum of normal random variables is also normally distributed. Consequently,

$$\dot{M}_t \sim \mathcal{N}\Big(\mathbb{E}(\dot{M}_t), \mathrm{Var}(\dot{M}_t)\Big) \tag{E7}$$

where the mean is

$$\mathbb{E}(\dot{M}_t) = \frac{1}{\delta t} \sum_{i=-\alpha}^{\alpha} \delta_{t+i}\mathbb{E}(M_{t+i}) \tag{E8}$$

and variance is

$$\mathrm{Var}(\dot{M}_t) = \frac{1}{(\delta t)^2}\Big[\sum_{i=-\alpha}^{\alpha}\delta_{t+i}^2\mathrm{Var}(M_{t+i}) + 2\sum_{i\neq j}\delta_{t+i}\delta_{t+j}\mathrm{Cov}(M_{t+i}, M_{t+j})\Big] = \frac{1}{(\delta t)^2}\sum_{i=-\alpha}^{\alpha}\delta_{t+i}^2\mathrm{Var}(M_{t+i}) \tag{E9}$$

where each covariance is zero because each measurement is independent. Because each $\dot{M}_t$ is normally distributed, this sequence of means and variances fully parameterizes its random process. To calculate k_t, we also must calculate $\mathrm{Cov}(M_t, \dot{M}_t)$:

$$\mathrm{Cov}(M_t, \dot{M}_t) = \frac{1}{\delta t}\mathbb{E}\Big[M_t \sum_{i=-\alpha}^{\alpha}\delta_{t+i}M_{t+i}\Big] - \frac{1}{\delta t}\mathbb{E}(M_t)\sum_{i=-\alpha}^{\alpha}\delta_{t+i}\mathbb{E}(M_{t+i})$$

$$= \frac{1}{\delta t}\sum_{i=-\alpha}^{\alpha}\delta_{t+i}\mathrm{Cov}(M_t, M_{t+i}) = \frac{1}{\delta t}\delta_t\mathrm{Var}(M_t) = 0 \tag{E10}$$

where the last two equalities follow from the independence of each M_t and the fact that the central coefficient (δ_t) in any
central finite difference for the first derivative is zero. For non-central differences, this is not zero, the last equality does not
hold, and $\mathrm{Cov}(M_t, \dot{M}_t) = \frac{1}{\delta t} \delta_t \mathrm{Var}(M_t)$.

With random processes for the mass and mass rate of change calculated we can calculate the decay rate coefficient as a
function of these two random processes:

$$k_t = -\frac{\dot{M}_t}{M_t} \tag{E11}$$

which is a ratio of two Gaussian random processes which may be correlated depending on the finite differencing scheme. The
calculation of such a ratio of random variables (Fieller, 1932; Hinkley, 1969) describes the uncertainty of the decay coefficient
at each time as a PDF $f_{k_t}(k)$.

Calculating the PDF for the instantaneous e-folding time $\tau_t = k_t^{-1}$ is performed by applying standard rules for functions of
random variables (from DeGroot and Schervish, 2012):

$$f_{\tau_t}(\tau) = \frac{1}{\tau^2} f_{k_t}\left(\frac{1}{\tau}\right). \tag{E12}$$

Notably, neither the distributions for decay rate coefficient nor for e-folding time are Gaussian.

Author contributions. DMH and MJP conceived of the main concepts. DMH developed the mathematical framework and details for the
probabilistic retrieval. DMH developed the code used to construct the background spectra and perform the retrieval. MJP performed all
radiative transfer modelling. MJP and DMH analyzed the sensitivity of the Jacobians and developed the specialized retrieval for strong
loading. DMH and MJP both tested and tuned the retrieval as well as interpreted and discussed the results. DMH and MJP wrote the
manuscript.

Competing interests. The authors declare no competing interests.

Acknowledgements. The NOAA JPSS Proving Ground and Risk Reduction (PGRR) Program funded this research (Federal Grant number:
NA15NES4320001). The authors wish to thank Lieven Clarrise for sharing the data used to construct the SO_2-free background timeline
as well as all members of the JPSS PGRR Volcanic Hazards Initiative team for feedback on product development. The views, opinions,
and findings contained in this report are those of the authors and should not be construed as an official National Oceanic and Atmospheric
Administration or U.S. Government position, policy, or decision.

References

Barzilai, J. and Borwein, J. M.: Two - Point Step Size Gradient Methods, IMA J Numerical Analysis, 8(1), 141–148,
655   https://doi.org/https://doi.org/10.1093/imanum/8.1.141, 1988.

Bauduin, S., Clarisse, L., Hadji-Lazaro, J., Theys, N., Clerbaux, C., and Coheur, P.-F.: Retrieval of near-surface sulfur diox-
ide (SO_2) concentrations at a global scale using IASI satellite observations, Atmospheric Measurement Techniques, 9, 721–740,
https://doi.org/10.5194/amt-9-721-2016, https://www.atmos-meas-tech.net/9/721/2016/, 2016.

Carboni, E., Grainger, R., Walker, J., Dudhia, A., and Siddans, R.: A new scheme for sulphur dioxide retrieval from IASI measurements:
660   application to the Eyjafjallajökull eruption of April and May 2010, Atmos Chem Phys, 12, 11 417–11 434, 2012.

Carboni, E., Grainger, R., Mather, T. A., Pyle, D. M., Thomas, G. E., Siddans, R., Smith, A. J. A., Dudhia, A., Koukouli, M. E., , and Balis,
D.: The vertical distribution of volcanic SO_2 plumes measured by IASI, Atmos Chem Phys, 16, 4343–4367, 2016.

Cario, M. C. and Nelson, B. L.: Modeling and Generating Random Vectors with Arbitrary Marginal Distributions and Correlation Matrix,
Tech. rep., Department of Industrial Engineering and Management Science, Northwestern University, Evanston, IL, http://citeseerx.ist.
665   psu.edu/viewdoc/summary?doi=10.1.1.48.281, 1997.

Carn, S. A., Krueger, A. J., Krotkov, N. A., Yang, K., and Evans, K.: Tracking volcanic sulfur dioxide clouds for aviation hazard mitigation,
Natural Hazards, 51, 325–343, https://doi.org/10.1007/s11069-008-9228-4, https://doi.org/10.1007/s11069-008-9228-4, 2009.

Carn, S. A., Fioletov, V. E., McLinden, C. A., Li, C., and Krotkov, N. A.: A decade of global volcanic SO2 emissions measured from space,
Scientific Reports, 7, 44 095, https://doi.org/10.1038/srep44095, https://doi.org/10.1038/srep44095, 2017.

670   Carn, S. A., Krotkov, N. A., Fisher, B. L., Li, C., and Prata, A. J.: First Observations of Volcanic Eruption Clouds From the L1 Earth-Sun
Lagrange Point by DSCOVR/EPIC, Geophysical Research Letters, 45, 11,456–11,464, https://doi.org/10.1029/2018GL079808, https:
//agupubs.onlinelibrary.wiley.com/doi/abs/10.1029/2018GL079808, 2018.

Casadevall, T. J.: The 1989-1990 eruption of Redoubt Volcano, Alaska: impacts on aircraft operations, Journal of Volcanology and Geother-
mal Research, 62, 301–316, https://doi.org/10.1016/0377-0273(94)90038-8, http://pubs.er.usgs.gov/publication/70017560, 1994.

675   Chin, M. and Jacob, D. J.: Anthropogenic and natural contributions to tropospheric sulfate: A global model analysis, Journal of Geophysi-
cal Research: Atmospheres, 101, 18 691–18 699, https://doi.org/10.1029/96JD01222, https://agupubs.onlinelibrary.wiley.com/doi/abs/10.
1029/96JD01222, 1996.

Clarisse, L., Coheur, P.-F., Theys, N., Hurtmans, D., and Clerbaux, C.: The 2011 Nabro eruption, a SO_2 plume height analysis using IASI
measurements, Atmos Chem Phys, 14, 3095–3111, 2014.

680   Clough, S. A. and Iacono, M. J.: Line-by-line calculation of atmospheric fluxes and cooling rates: 2. Application to carbon diox-
ide, ozone, methane, nitrous oxide and the halocarbons, Journal of Geophysical Research: Atmospheres, 100, 16 519–16 535,
https://doi.org/10.1029/95JD01386, https://agupubs.onlinelibrary.wiley.com/doi/abs/10.1029/95JD01386, 1995.

Coombs, M., Wallace, K., Cameron, C., Lyons, J., Wech, A., Angeli, K., and Cervelli, P.: Overview, chronology, and impacts of the 2016–
2017 eruption of Bogoslof volcano, Alaska, Bulletin of Volcanology, 81, 62, https://doi.org/10.1007/s00445-019-1322-9, https://doi.org/
685   10.1007/s00445-019-1322-9, 2019.

Coombs, M. L., Wech, A. G., Haney, M. M., Lyons, J. J., Schneider, D. J., Schwaiger, H. F., Wallace, K. L., Fee, D., Freymueller, J. T., Schae-
fer, J. R., and Tepp, G.: Short-Term Forecasting and Detection of Explosions During the 2016–2017 Eruption of Bogoslof Volcano, Alaska,
Frontiers in Earth Science, 6, 122, https://doi.org/10.3389/feart.2018.00122, https://www.frontiersin.org/article/10.3389/feart.2018.00122,
2018.

690 Corradini, S., Merucci, L., Prata, A. J., and Piscini, A.: Volcanic ash and SO2 in the 2008 Kasatochi eruption: Retrievals comparison
        from different IR satellite sensors, Journal of Geophysical Research: Atmospheres, 115, https://doi.org/10.1029/2009JD013634, https:
        //agupubs.onlinelibrary.wiley.com/doi/abs/10.1029/2009JD013634, 2010.

    DeGroot, M. H. and Schervish, M. J.: Probability and statistics, 4th Edition, Boston Pearson Education, http://openlibrary.org/books/
        OL24039868M, 2012.

695 Fieller, E. C.: The Distribution of the Index in a Normal Bivariate Population, Biometrika, 24, 428–440, http://www.jstor.org/stable/2331976,
        1932.

    Gambacorta, A.: The NOAA Unique CrIS/ATMS Processing System (NUCAPS): Algorithm Theoretical Basis Documentation,
        https://www.ospo.noaa.gov/Products/atmosphere/soundings/nucaps/docs/NUCAPS_ATBD_20130821.pdf, 2013.

    Guffanti, M., Schneider, D. J., Wallace, K. L., Hall, T., Bensimon, D. R., and Salinas, L. J.: Aviation response to a widely dispersed volcanic

700   ash and gas cloud from the August 2008 eruption of Kasatochi, Alaska, USA, Journal of Geophysical Research: Atmospheres, 115,
        https://doi.org/10.1029/2010JD013868, https://agupubs.onlinelibrary.wiley.com/doi/abs/10.1029/2010JD013868, 2010.

    Han, Y., Revercomb, H., Cromp, M., Gu, D., Johnson, D., Mooney, D., Scott, D., Strow, L., Bingham, G., Borg, L., Chen, Y., DeSlover,
        D., Esplin, M., Hagan, D., Jin, X., Knuteson, R., Motteler, H., Predina, J., Suwinski, L., Taylor, J., Tobin, D., Tremblay, D., Wang, C.,
        Wang, L., Wang, L., and Zavyalov, V.: Suomi NPP CrIS measurements, sensor data record algorithm, calibration and validation activities,

705   and record data quality, Journal of Geophysical Research: Atmospheres, 118, 12,734–12,748, https://doi.org/10.1002/2013JD020344,
        https://agupubs.onlinelibrary.wiley.com/doi/abs/10.1002/2013JD020344, 2013.

    Hedelt, P., Efremenko, D., Loyola, D., Spurr, R., and Clarisse, L.: Sulfur dioxide layer height retrieval from Sentinel-5 Precursor/TROPOMI
        using FP-ILM, Atmospheric Measurement Techniques, 12, 5503–5517, https://doi.org/10.5194/amt-12-5503-2019, 2019.

    Hinkley, D. V.: On the Ratio of Two Correlated Normal Random Variables, Biometrika, 56, 635–639, http://www.jstor.org/stable/2334671,

710   1969.

    International Civil Aviation Organization (ICAO): Flight safety and volcanic ash, http://www.icao.int/publications/Documents/9974_en.pdf,
        2012.

    Karagulian, F., Clarisse, L., Clerbaux, C., Prata, A. J., Hurtmans, D., and Coheur, P. F.: Detection of volcanic SO2, ash, and
        H2SO4 using the Infrared Atmospheric Sounding Interferometer (IASI), Journal of Geophysical Research: Atmospheres, 115,

715   https://doi.org/10.1029/2009JD012786, https://agupubs.onlinelibrary.wiley.com/doi/abs/10.1029/2009JD012786, 2010.

    Krotkov, N. A., Schoeberl, M. R., Morris, G. A., Carn, S., and Yang, K.: Dispersion and lifetime of the SO2 cloud from the August
        2008 Kasatochi eruption, Journal of Geophysical Research: Atmospheres, 115, https://doi.org/10.1029/2010JD013984, https://agupubs.
        onlinelibrary.wiley.com/doi/abs/10.1029/2010JD013984, 2010.

    Li, C., Krotkov, N. A., Carn, S., Zhang, Y., Spurr, R. J. D., and Joiner, J.: New-generation NASA Aura Ozone Monitoring Instrument (OMI)

720   volcanic SO$_2$ dataset: algorithm description, initial results, and continuation with the Suomi-NPP Ozone Mapping and Profiler Suite
        (OMPS), Atmospheric Measurement Techniques, 10, 445–458, https://doi.org/10.5194/amt-10-445-2017, https://www.atmos-meas-tech.
        net/10/445/2017/, 2017.

    Moxnes, E. D., Kristiansen, N. I., Stohl, A., Clarisse, L., Durant, A., Weber, K., and Vogel, A.: Separation of ash and sulfur dioxide during
        the 2011 Grímsvötn eruption, Journal of Geophysical Research: Atmospheres, 119, 7477–7501, https://doi.org/10.1002/2013JD021129,

725   https://agupubs.onlinelibrary.wiley.com/doi/abs/10.1002/2013JD021129, 2014.

Pavolonis, M. J.: Advances in Extracting Cloud Composition Information from Spaceborne Infrared Radiances—A Robust Alternative to Brightness Temperatures. Part I: Theory, Journal of Applied Meteorology and Climatology, 49, 1992–2012, https://doi.org/10.1175/2010JAMC2433.1, https://doi.org/10.1175/2010JAMC2433.1, 2010.

Pavolonis, M. J., Heidinger, A. K., and Sieglaff, J.: Automated retrievals of volcanic ash and dust cloud properties from upwelling infrared measurements, Journal of Geophysical Research: Atmospheres, 118, 1436–1458, https://doi.org/10.1002/jgrd.50173, https://agupubs.onlinelibrary.wiley.com/doi/abs/10.1002/jgrd.50173, 2013.

Pavolonis, M. J., Sieglaff, J., and Cintineo, J.: Spectrally Enhanced Cloud Objects—A generalized framework for automated detection of volcanic ash and dust clouds using passive satellite measurements: 1. Multispectral analysis, Journal of Geophysical Research: Atmospheres, 120, 7813–7841, https://doi.org/10.1002/2014JD022968, https://agupubs.onlinelibrary.wiley.com/doi/abs/10.1002/2014JD022968, 2015a.

Pavolonis, M. J., Sieglaff, J., and Cintineo, J.: Spectrally Enhanced Cloud Objects—A generalized framework for automated detection of volcanic ash and dust clouds using passive satellite measurements: 2. Cloud object analysis and global application, Journal of Geophysical Research: Atmospheres, 120, 7842–7870, https://doi.org/10.1002/2014JD022969, https://agupubs.onlinelibrary.wiley.com/doi/abs/10.1002/2014JD022969, 2015b.

Pavolonis, M. J., Sieglaff, J., and Cintineo, J.: Automated Detection of Explosive Volcanic Eruptions Using Satellite-Derived Cloud Vertical Growth Rates, Earth and Space Science, 5, 903–928, https://doi.org/10.1029/2018EA000410, https://agupubs.onlinelibrary.wiley.com/doi/abs/10.1029/2018EA000410, 2018.

Prata, A. J.: Satellite detection of hazardous volcanic clouds and the risk to global air traffic, Natural Hazards, 51, 303–324, https://doi.org/10.1007/s11069-008-9273-z, https://doi.org/10.1007/s11069-008-9273-z, 2009.

Prata, F. and Rose, B.: Chapter 52 - Volcanic Ash Hazards to Aviation, in: The Encyclopedia of Volcanoes (Second Edition), edited by Sigurdsson, H., pp. 911 – 934, Academic Press, Amsterdam, second edition edn., https://doi.org/https://doi.org/10.1016/B978-0-12-385938-9.00052-3, http://www.sciencedirect.com/science/article/pii/B9780123859389000523, 2015.

Read, W. G., Froidevaux, L., and Waters, J. W.: Microwave limb sounder measurement of stratospheric SO2 from the Mt. Pinatubo Volcano, Geophysical Research Letters, 20, 1299–1302, https://doi.org/10.1029/93GL00831, https://agupubs.onlinelibrary.wiley.com/doi/abs/10.1029/93GL00831, 1993.

Robock, A.: Volcanic eruptions and climate, Reviews of Geophysics, 38, 191–219, https://doi.org/10.1029/1998RG000054, https://agupubs.onlinelibrary.wiley.com/doi/abs/10.1029/1998RG000054, 2000.

Rodgers, C. D.: Inverse Methods for Atmospheric Sounding: Theory and Practice, World Scientific, River Edge, N. J., 2000.

Schneider, D., Van Eaton, A. R., and Wallace, K.: Satellite observations of the 2016–17 eruption of Bogoslof volcano: aviation and ash fallout hazard implications from a water-rich eruption, Bulletin of Volcanology, *in press*, 2020.

Sears, T. M., Thomas, G. E., Carboni, E., A. Smith, A. J., and Grainger, R. G.: SO2 as a possible proxy for volcanic ash in aviation hazard avoidance, Journal of Geophysical Research: Atmospheres, 118, 5698–5709, https://doi.org/10.1002/jgrd.50505, https://agupubs.onlinelibrary.wiley.com/doi/abs/10.1002/jgrd.50505, 2013.

Sekiya, T., Sudo, K., and Nagai, T.: Evolution of stratospheric sulfate aerosol from the 1991 Pinatubo eruption: Roles of aerosol microphysical processes, Journal of Geophysical Research: Atmospheres, 121, 2911–2938, https://doi.org/10.1002/2015JD024313, https://agupubs.onlinelibrary.wiley.com/doi/abs/10.1002/2015JD024313, 2016.

Sennert, S. K.: Report on Raikoke (Russia), Weekly Volcanic Activity Report, 19 June - 25 June 2019, Global Volcanism Program, Smithsonian Institution and US Geological Survey, 2019.

Theys, N., Campion, R., Clarisse, L., Brenot, H., van Gent, J., Dils, B., Corradini, S., Merucci, L., Coheur, P.-F., Van Roozendael,
M., Hurtmans, D., Clerbaux, C., Tait, S., and Ferrucci, F.: Volcanic SO$_2$ fluxes derived from satellite data: a survey using OMI,
GOME-2, IASI and MODIS, Atmospheric Chemistry and Physics, 13, 5945–5968, https://doi.org/10.5194/acp-13-5945-2013, https:
//www.atmos-chem-phys.net/13/5945/2013/, 2013.

Theys, N., Hedelt, P., De Smedt, I., Lerot, C., Yu, H., Vlietinck, J., Pedergnana, M., Arellano, S., Galle, B., Fernandez, D., Carlito, C. J. M.,
Barrington, C., Taisne, B., Delgado-Granados, H., Loyola, D., and Van Roozendael, M.: Global monitoring of volcanic SO2 degassing
with unprecedented resolution from TROPOMI onboard Sentinel-5 Precursor, Scientific Reports, 9, 2643, https://doi.org/10.1038/s41598-
019-39279-y, https://doi.org/10.1038/s41598-019-39279-y, 2019.

Turner, D. D.: Arctic Mixed-Phase Cloud Properties from AERI Lidar Observations: Algorithm and Results from SHEBA, Journal of Applied
Meteorology, 44, 427–444, https://doi.org/10.1175/JAM2208.1, https://doi.org/10.1175/JAM2208.1, 2005.

Vasconez, F., Ramón, P., Hernandez, S., Hidalgo, S., Bernard, B., Ruiz, M., Alvarado, A., La Femina, P., and Ruiz, G.: The differ-
ent characteristics of the recent eruptions of Fernandina and Sierra Negra volcanoes (Galápagos, Ecuador), Volcanica, 1, 127 – 133,
https://doi.org/10.30909/vol.01.02.127133, https://doi.org/10.30909/vol.01.02.127133, 2018.

Walker, J. C., Dudhia, A., and Carboni, E.: An effective method for the detection of trace species demonstrated using the MetOp Infrared
Atmospheric Sounding Interferometer, Atmos Meas Tech, 4, 1567–1580, 2011.

Walker, J. C., Carboni, E., Dudhia, A., and Grainger, R. G.: Improved detection of sulphur dioxide in volcanic plumes using satellite-based
hyperspectral infrared measurements: Application to the Eyjafjallajökull 2010 eruption, Journal of Geophysical Research: Atmospheres,
117, https://doi.org/10.1029/2011JD016810, https://agupubs.onlinelibrary.wiley.com/doi/abs/10.1029/2011JD016810, 2012.

Zavyalov, V., Esplin, M., Scott, D., Esplin, B., Bingham, G., Hoffman, E., Lietzke, C., Predina, J., Frain, R., Suwinski, L., Han, Y., Major,
C., Graham, B., and Phillips, L.: Noise performance of the CrIS instrument, Journal of Geophysical Research: Atmospheres, 118, 13,108–
13,120, https://doi.org/10.1002/2013JD020457, https://agupubs.onlinelibrary.wiley.com/doi/abs/10.1002/2013JD020457, 2013.